Innovative use of low-frequency ultrasound for particle separation/classification : Forces acting on a single particle held in water of 20-kHz-ultrasound pressure fields in transition states under control of the acoustic pressure amplitude

Research Article

Innovative use of low-frequency ultrasound for particle separation/classification: Forces acting on a single particle held in water of 20-kHz-ultrasound pressure fields in transition states under control of the acoustic pressure amplitude

Hiroya Muramatsu Mizutani[1] and Takayuki Saito[2,*]

[1]Graduate School of Science and Technology, and [2]Research Institute of Green Science and Technology, Shizuoka University, 3-5-1 Johoku, Naka-ku, Hamamatsu, Shizuoka 4328561, Japan

***Corresponding author:** Prof. Takayuki Saito, Research Institute of Green Science and Technology, Shizuoka University, 3-5-1 Johoku, Naka-ku, Hamamatsu, Shizuoka 4328561, Japan. Tel. & Fax: +81-53-478-1601. Email: saito.takayuki@shizuoka.ac.jp

H.M. Mizutani: muramatsu.hiroya.15@shizuoka.ac.jp

Abstract

We have developed a unique particle-separation technique based on size that uses kHz-band ultrasound irradiation in water. Dispersed-millimeter-size particles in dissolved-gases water form themselves into a spherically flocculated particle swarm (SFPS). With the changes of ultrasound irradiation properties, the particles are separated according to their sizes. We previously investigated the characteristics of an SFPS and elucidated its formation mechanism. To achieve an efficient and precise particle-separation technique, the forces acting on the particles during the transition state of the ultrasound modulation must be determined, but it is difficult to clarify the forces acting on each particle. Herein, we experimentally and systematically investigated the forces acting on a single particle trapped in the sound pressure field. We discuss nine types of forces acting on the particle and the bubble adhering to its surface. Under the static state, the particle buoyancy was counterbalanced with the acoustic radiation force acting on the acoustic cavitation-oriented bubbles (ACOBs). We examined two types of amplitude change: a gradual amplitude change of the input power of a transducer, and a step-like amplitude change. The results revealed that the particle motion depends on a subtle balance between the acoustic radiation force acting on the ACOBs and unsteady fluid-dynamical forces acting on the particle. We also demonstrate the classification of particles by diameter by controlling the transition state of the amplitude change of the ultrasound input power. We conclude that the gradual amplitude change provided an efficient and precise classification of particles by their diameters.

Keywords

kHz-ultrasound, acoustic cavitation-oriented bubble, separation, particle image velocimetry

Abbreviations

ACOB: acoustic cavitation-oriented bubble

SFPS: spherically flocculated particle swarm

LPAR: large-pressure amplitude region

SPAR: small-pressure amplitude region

Highlights

- We investigated the forces acting on a particle trapped in a sound pressure field.
- The gravity on a particle and acoustic radiation force acting on ACOB are balanced.
- The dominant forces were not changed by the gradual change of input power.
- The dominant forces were changed by the step-like change of input power.
- The gradual amplitude change is suitable for particle separation by size.

1. Introduction

Ultrasound techniques for the separation of particles have shown promise in part because of their advantages: noncontact separation and a simple apparatus. Conventional ultrasound particle-separation techniques use the acoustic radiation force that acts directly on separation targets, and these techniques therefore use mostly MHz-band ultrasound due to its high directionality and strong acoustic radiation force. For example, Woodside and Piret (1998) estimated the acoustic radiation force acting on 10.2-μm-dia. polystyrene particles in water under 2.2 MHz ultrasound irradiation. However, MHz-band ultrasound separation techniques have a particle size limitation that is related to the mechanism of trapping particles (i.e., the primary radiation force aggregates the particles in nodal planes); the particles must be smaller than the wavelength of the standing wave generated in the medium.

Several research groups have used kHz-band ultrasound for particle separation and manipulation. Ochiai et al. (2014) reported that they succeeded in the manipulation of polystyrene particles (PSPs) of several millimeters in diameter in air by using 40-kHz-ultrasound arrays. Kozuka et al. (2007) successfully manipulated 2–3-mm-dia. PSPs confined in an air-filled space between two ultrasound transducers in an opposed arrangement. The number of manipulated particles in those two studies (1–50) was small. For the establishment of ultrasound separation methods as next-generation separation techniques, the manipulation of large numbers of particles must be achieved with a simple and reasonable apparatus.

We discovered an intriguing phenomenon in which approx. 1-mm-dia. PSPs dispersed in water formed themselves into a spherically flocculated particle swarm (SFPS) by irradiating 20-kHz ultrasound (Mizushima et al. 2013). Our previous studies regarding the characteristics of the SFPS as well as the flocculation mechanism can be summarized as

follows. The SFPS stayed at a large-pressure amplitude region (LPAR) in water (Muramatsu et al. 2015). Acoustic cavitation-oriented bubbles (ACOBs) play an essential role in the formation of the SFPS. The ACOBs adhered to the particle surface and led the particles toward the LPAR (Mizushima et al. 2013). The acoustic radiation force acting on the ACOBs is a dominant force for transporting the particles and holding the SFPS in the water (Muramatsu and Saito 2017). This ultrasound technique provides a way to manipulate the SFPS via a simple apparatus: by inserting a motion-controlled stick in the vicinity of the SFPS, we can easily manipulate the SFPS three-dimensionally by moving the stick (Yanai and Saito 2017; Muramatsu and Saito 2018). We also proposed a new particle classification process based on particle diameter that is achieved by precisely controlling the ultrasound amplitude and frequency (Muramatsu et al. 2015; Muramatsu and Saito 2018).

For example, in order to develop a cesium decontamination system using Prussian blue particles for the specific purpose of volume reduction, an innovative particle classification process based on small differences in the density of particles is needed. Parajuli et al. (2016) reported that the adsorption efficiency of cesium differed by the size of secondary Prussian blue particles composed of Prussian blue nanoparticles. The differences in the particle mass by the particle diameter are larger than the differences in the particle density by the cesium adsorption. For this reason, the new system must classify the particles via two processes.

At the present phase, we propose the following decontamination process using the secondary Prussian blue particles. The first process precisely classifies and separates the particles by their diameters; the particles that have high adsorption efficiency are thus obtained. After the cesium adsorption process, the mass of Prussian blue particles that have fully adsorbed cesium increases. The second process classifies and separates the processed particles by the density, in association with differences in fluid-dynamical forces (e.g., drag

force, virtual mass force and Basset force) caused by the density difference. In both the first and second processes, the subtle control of both the ultrasound power and separated-particle manipulation is needed. It is thus necessary to determine the forces acting on the particles inside the SFPS, which is held at both a stationary position and a traversing position in the sound pressure field.

However, evaluating the forces acting on the flocculating particles inside an SFPS is very difficult at the present time. In our careful observations of the SFPS, the diameter and shape of the SFPS changed periodically; i.e., the particles composing the SFPS moved restlessly in an area of the maximum circumscribed sphere of the SFPS; the maximum diameter of the circumscribed sphere was estimated as approx. 13 mm. In other words, the particles move in the LPAR, where the pressure amplitude changes spatially and sharply. In consideration of the above observations, we rendered an evaluation of the forces acting on the flocculating particles inside an SFPS into an evaluation of the forces acting on a particle moving in an area near the LPAR under constant or controlled ultrasound irradiation.

We conducted the present study to determine how to precisely control the particle separation by clarifying the forces acting on a particle held in the sound pressure field. We first investigated the relationship between a trapped PSP and its sound pressure distribution under the static state of the input power to the ultrasound transducer, as the basis of the manipulation control of PSPs. We evaluated the forces acting on the trapped PSP near the LPAR in a simultaneous visualization of the PSP's motion and its surrounding liquid motion. Second, by examining two types of amplitude change in the input power (gradual change and step-like change), we discuss the influence of the input power change on the PSP's motion in an analysis of the forces acting on the PSP. We consider the influence of the rate of the amplitude change on the PSP's motion, and we elucidate the differences in the dominant forces between the gradual input power change and the step-like amplitude change.

Third, on the basis of the obtained results, we demonstrate the particle classification process based on particle diameter, under both the gradual and step-like changes of the input power. Finally, we propose the optimal sound pressure control for a precise particle separation/classification technique.

2. Experimental setup

2.1. The force analysis procedure

Figure 1 is a typical snapshot of the visualization result of the surface oscillation of an ACOB that adheres to an acoustically trapped particle surface. We considered the following forces acting on the particle and ACOB. F_{Pg}, the gravitational and buoyancy force acting on the particle; F_{Bg}, the buoyancy force acting on the ACOB; F_{Pd}, the fluid drag acting on the particle; F_{Pv}, the added (virtual) mass force acting on the particle; F_{Pp}, the pressure gradient force acting on the particle; F_{Ph}, the Basset history force acting on the particle; F_{Pa}, the acoustic radiation force acting on the particle; F_{Ba}, the acoustic radiation force acting on the ACOB; and F_T, the total force acting on the trapped particle system. Figure 2 provides a flowchart of the force analysis in the present study.

— Place Fig. 1 here —

— Place Fig. 2 here —

First, we calculated F_{Pg}, and F_{Bg}, which are calculated using the ACOB visualization results. Second, on the basis of Equations (1) and (2) (Gor'kov's equation, Gor'kov 1962), we numerically calculated F_{Pa} as a function of the square of the input power to an ultrasound transducer.

$$F_{Pa} = 4\pi E \left(\frac{D_P}{2}\right)^2 \left(k\frac{D_P}{2}\right) \sin 2kz \left\{\frac{\rho_P + {}^2/_3(\rho_P - \rho_L)}{2\rho_P + \rho_L} - \frac{1}{3}\frac{\rho_P c_P^2}{\rho_L c_L^2}\right\}, \quad (1)$$

$$E = \frac{p^2}{4\rho_L c_L^2}, \quad (2)$$

where E is the average energy density of acoustical energy, and k is the wave number. Third, we processed high-speed-video images of the single polystyrene particle (PSP) and particle image velocimetry (PIV) tiny seeding particles (PIV particles) through the binary and area processes and divided them into PSP images (PSPIs) and PIV images (PIVIs). Fourth, we analyzed the center-gravity velocity u_P of the PSP, from the PSPIs.

Fifth, the PSP's surrounding liquid-phase velocity u_L was calculated via a PIV process (PIV algorithm: a fast Fourier transform [FFT]-based recursive cross-correlation method, Saito et al., 2010). From this result, we estimated the pressure gradient force F_{Pp}. Sixth, we calculated the relative velocity u_{Pr} between u_P and u_L, and we estimated the drag force F_{Pd}, the added mass force F_{Pv}, the Basset history force F_{Ph}, and the total force F_T. Finally, we estimated F_{Ba} by the subtraction of other forces from F_T. In the present study, we estimated u_P, u_L, and the forces in the z-direction, since the PSP moved mainly vertically. To execute the above calculation procedure rationally, we designed and made the experimental setup described below.

2.2. Simultaneous visualization of both the particle motion and its surround liquid motion

Figure 3 is a schematic of the experimental setup for the simultaneous visualization of the trapped particle motion and liquid motion. The experimental setup was separated into two devices: the driving device and the visualization device. The sinuous signal from a function generator (SG-4332, Iwatsu, Tokyo) was amplified through an amplifier (2100L,

E&I, Rochester, NY). The amplified signal was inputted to a bolt-clamped Langevin-type (BLT) transducer (HEM-45254M, Honda Electronics, Toyohashi, Japan) through an impedance matching circuit. The BLT transducer was strongly bonded to a stainless-steel plate (thickness: 3 mm). The plate was fixed to the bottom of an acrylic vessel (inner size: 54×54×150 mm, thickness: 3 mm).

Air-saturated deionized water was poured into the vessel to 120-mm depth. The concentrations of the dissolved gases were measured through a dissolved O_2 meter (HT2040-01, Hanna Instruments, Tokyo) and a CO_2 meter (CGP-31, DKK-TOA, Tokyo). The gas concentrations were 0.03 mM/L (O_2) and 0.26 mM/L (CO_2), respectively. A sound pressure field developed rapidly and grew in the vessel by the ultrasound irradiated from the bottom of the vessel. We used a 1-mm-dia. PSP (density: 1060 kg/m^3, particle Reynolds number: 15.0). The PSP attaching an ACOB on its surface was held in the vessel under the ultrasound irradiation. The irradiation frequency was set at 20.3 kHz, and the voltage of the function generator was controlled arbitrarily. To determine the effects of particle motion on the change rate of the sound pressure, we investigated two types of input power change, i.e., step-like and gradual changes.

To clearly visualize the motions of both the particle and its surrounding liquid, we used a combined visualization technique: a shadowgraph for the PSP's motion and PIV for the liquid motion. As shown in Figure 3, we defined an *x*-*y*-*z* coordinate system with the center of the vessel bottom as the coordinate origin. Both the PSP's motion and liquid motion on an *x*-*z* plane were filmed. A high-speed camera (FASTCAM SA-X2, Photron, Yonezawa, Japan) and a flat LED light (HF-SL-100WLCG, Raytronics, Saitama, Japan) were mounted facing each other on optical stages.

For the visualization of the liquid motion, we seeded PIV particles (fluorescence particles with 532-nm excitation wavelength and 570-nm emission wavelength, Fluoro-

Max™, Thermo Fisher Scientific, Waltham, MA; dia. 8 μm, density 1020 kg/m^3) into the vessel. In our previous study (Muramatsu and Saito 2017), the PIV particles were not flocculated even under ultrasound irradiation into degassed water, furthermore, no water currents were observed in the degassed water. In the present study, the diameter of the PIV particle was 8 μm; this diameter was much smaller than the wavelength of the stationary wave. In the light of these published results and common knowledge regarding acoustic radiation forces, the acoustic radiation force directly acting on the water was negligibly small. The SFPS formed in water with the dispersed PIV particles was extremely similar to that observed in water without the PIV particles. We thus considered the influences of the PIV particles on the sound pressure field were also negligibly small. The PIV particles were small enough to be unaffected by the acoustic radiation forces. A laser beam sheeted by a rod lens illuminated an interrogation area from the side of the vessel (*x*-*z* plane).

For the simultaneous visualization of the PSP and the emission light from the PIV particles, we installed a high-pass filter (SCF-50S-54, Sigmakoki) in front of the camera lens. The settings of the camera were as follows: image size 1024×1024 pixels, frame rate 2000 fps, exposure time 0.5 msec, and spatial resolution 20.2 μm/pixel. The signals from each type of equipment were stored in digital recorder (Recorder #8861-50, A/D converter #8965; Hioki, Nagano, Japan).

Since the ACOB's size and surface oscillation were smaller and faster than the PSP's motion, we visualized the ACOB by using a metal halide lamp (MME-250; Moritex, Saitama, Japan) that emitted stronger light than the LED light. The camera settings were as follows: image size 1024×1024 pixels, frame rate 7200 fps, exposure time 10 μsec, and spatial resolution 6.25 μm/pixel.

— Place Fig. 3 here —

3. Results and Discussion

3.1. The PSP's stationary position during the amplitude change of the acoustic power

We investigated the sound pressure profile in the vessel, and here we discuss the influence of the input power P_{in} on the sound pressure profile after Muramatsu and Saito (2018). The dominant wavelength of the sound pressure profile equaled the wavelength of the irradiated ultrasound frequency calculated from $\lambda = c_W/f$. The positions of the local maximum/minimum values of the sound pressure profile were not shifted by our variation of the input power. The sound pressure amplitude of the local maximum/minimum values increased with the increase in the input power.

The PSP's stationary position varying with the input power is plotted in Figure 4a (the range of the irradiation intensity in the present study was 0.031-0.086 W/cm^2). The PSP was trapped between the upper LPAR and SPAR (small-pressure amplitude region) at the center axis of the vessel. At $P_{in} = 2.12$ W (white square, Fig. 4a), the PSP kept its trapped position at $z = 72$ mm for a long time: the forces acting on the PSP were balanced. The stationary position of the PSP ascended with the decrease in P_{in}. A further decrease ($P_{in} = 1.09$ W) in the amplitude brought the PSP to an LPAR ($z = 85$ mm). At $P_{in} = 0.79$ W, the PSP's position fluctuated near the LPAR. The ACOB's diameter at $P_{in} = 0.79$ W (white circle, Fig. 4a) was larger than that at $P_{in} = 1.09$ W (gray circle, Fig. 4a). We discuss the reasons for these results on the basis of the forces acting on the PSP and ACOB, as follows.

— Place Fig. 4 here —

3.1.1. Estimation of F_{Pg} (the gravitational and buoyancy force acting on the PSP) and F_{Bg} (the buoyancy force acting on the ACOB)

First, F_{Pg} was calculated by the following equation:

$$F_{Pg} = (\rho_w - \rho_P) g V_P. \quad (3)$$

Here, the volume of the PSP, i.e., V_P, was calculated as 0.523 mm^3. F_{Pg} was calculated as −0.308 μN. Based on the visualization results, we plotted the diameter of the ACOB adhering to the PSP's surface (Fig. 5a). The ACOB oscillated to the irradiated ultrasound. The maximum and root mean square diameters were approx. 100 μm and 72 μm, respectively. F_{Bg} was calculated by the following equation:

$$F_{Bg} = \rho_w g V_B. \quad (4)$$

The buoyancy of the ACOB taking its maximum diameter was calculated at 0.005 μN. The maximum ratio of F_{Bg} to F_{Pg} in the present study was <2% (black circle, Fig. 5b); the contribution of F_{Bg} to the PSP's motion was not dominant.

— Place Fig. 5 here —

3.1.2. Estimation of F_{Pa} (the acoustic radiation force acting on the PSP)

In the present study, the PSP was held on the center-axis of the transducer. Gor'kov (1962) presented the equations calculating the acoustic radiation force acting on a particle in a sound pressure field without the existence of cavitation-oriented bubbles. The sound pressure amplitude near the PSP was unknown in the present study due to the assumed change of the sound pressure profile by the occurrence of the ACOBs. Simplifying Gor'kov's equations as shown below, in the present study we regarded F_{Pa} as a function of the sound pressure amplitude:

$$F_{Pa} = -2kEV_P \left\{ B(\rho) + 1 - \frac{\rho_L c_L^2}{\rho_P c_P^2} \right\}, \quad (5)$$

$$B(\rho) = \frac{3(1-\rho_L/\rho_P)}{2+\rho_L/\rho_P} \quad . \tag{6}$$

Mitome (2001) summarized the direction of an acoustic radiation force acting on a particle and a bubble; the particle was moved toward nodes (SPAR) by the acoustic radiation force, and the bubble was moved toward anti-nodes (LPAR) by the acoustic radiation force. Matula et al. (1997) reported a relationship between the sound pressure amplitude and the direction of an acoustic radiation force acting on bubbles. These bubbles moved toward nodes when the sound pressure amplitude was >180 kPa; this was caused by the integral of the forces toward nodes/anti-nodes during one cycle of the ultrasound irradiation period. In our flocculation technique, an SFPS was trapped at the LPAR, and the PSP was held between the LPAR and SPAR; the maximum sound pressure amplitude in the present study was thus <180 kPa.

In this study, the acoustic radiation force acted on not only the ACOB but also the trapped PSP. The PSP was forced to be held in the SFPS by F_{Pg} and F_{Pa}, which acted downwardly on the PSP. The PSP was thus trapped near the SPAR even when the sound pressure amplitude was smaller than Matula's criteria. As shown in Figure 4a, the PSP's stationary position was shifted out from the LPAR when the input power P_{in} was >1.41 W. Since the PSP departed from the LPAR in association with the increase in P_{in}, the acoustic radiation force acting on the ACOB might become smaller even though P_{in} increased. We assumed that the maximum sound pressure amplitude at P_{in} = 1.75 W was 120 kPa, which is two-thirds of Matula's criteria regarding the sound pressure amplitude. As shown in Figure 4b, the PSP's stationary position in the *z*-direction was 74 mm under this condition, and the sound pressure amplitude near the PSP was approx. 90% of the maximum sound pressure amplitude.

Therefore, at P_{in} = 1.75 W, a value of 100 kPa near the PSP was presumed as the

critical sound pressure amplitude. The acoustic radiation force acting on the PSP at $P_{in,c}$ (i.e., $F_{Pa,c}$) was calculated by Eqs. (5) and (6). F_{Pa} was then proportional to the square of the input power P_{in}. We thus calculated F_{Pa} by the following equation:

$$F_{Pa} = \left(\frac{P_{in}}{P_{in,c}}\right)^2 F_{Pa,c} \quad . \tag{7}$$

The numerical results are plotted in Figure 6. The acoustic radiation force acting directly on the PSP under $P_{in,c}$ was estimated at −0.033 μN; therefore, the ratio of $F_{Pa,c}$ to F_{Pg} was estimated at 10.7%.

— Place Fig. 6 here —

3.1.3. Estimation of the pressure gradient force F_{Pp}, drag force F_{Pd}, added mass force F_{Pv}, Basset history force F_{Ph}, and total force F_T

We analyzed both the PSP's motion and its surrounding liquid motion from the simultaneous visualization results. The liquid motion around the PSP was extracted by referring to the PSPIs. From the extracted two-dimensional liquid motion, we estimated the pressure gradient force acting on the PSP from Eq. (8):

$$F_{Pp} = \rho_W V_P \frac{du_L}{dt}. \tag{8}$$

Next, the relative velocity between the PSP and its surrounding liquid motion was calculated by Eq. (9):

$$u_{Pr} = u_L - u_P. \tag{9}$$

The Reynolds number Re and the drag coefficient C_D were thus calculated. As described

below, the range of *Re* values in the present study was <20. After Clift et al. (1978), we calculated the C_D by the following equation:

$$C_D = \frac{24}{Re}\left(1 + 0.1315Re^{(0.82-0.05\log_{10} Re)}\right). \quad (10)$$

The drag force F_{Pd} to the PSP was calculated as:

$$F_{Pd} = \frac{1}{2}\rho_L C_D S_P |u_{Pr}| u_{Pr}. \quad (11)$$

The virtual mass coefficient C_V was set at 0.5, because the PSP was a sphere, and F_{Pv} was calculated as:

$$F_{Pv} = C_V \rho_L V_P \left(\frac{du_L}{dt} - \frac{du_P}{dt}\right) = \frac{1}{2}\rho_W V_P \left(\frac{du_L}{dt} - \frac{du_P}{dt}\right). \quad (12)$$

The Basset history force originates in unsteady diffusion of vorticity in the vicinity of a particle. The *Re* in the present study was small (<20). We thus considered the Basset history force F_{Ph}. We calculated F_{Ph} as follows:

$$F_{Ph} = \frac{3}{2} D_P^2 \sqrt{\pi \rho_L \mu_L} \int_0^t \left(\frac{du_L}{d\tau} - \frac{du_P}{d\tau}\right) \frac{d\tau}{\sqrt{t-\tau}}. \quad (13)$$

Finally, the total force was calculated by the following equation:

$$F_T = \rho_P V_P \frac{du_P}{dt}. \quad (14)$$

The experimental results at P_{in} = 1.75 W during the *t* of 0 to 0.5 sec are shown in Figure 7. The time-series of the PSP's position in the *z*-direction is plotted in Figure 7a. The

PSP ascended slightly. The standard deviation of the PSP's position was 0.17 mm. The PSP velocity u_P and its surrounding liquid velocity u_L are plotted in Figure 7b. The u_L value at $t = 0.1$ s was 0.17 mm/sec, and the u_p was 0.89 mm/sec, which is five times as large as u_L. The fluctuation of the liquid velocity was small; therefore the liquid motion was considered to be temporally stable.

F_{Pp} was negligible due to the small acceleration/deceleration of the liquid motion near the PSP. The calculated forces (F_T, F_{Pd}, F_{Ph}, F_{Pv}, F_{Pp}, and F_{Bg}) are plotted in Figure 7c. F_{Pd} at $t = 0$ sec was calculated as −0.080 μN, and it was the dominant force among these forces. With the decrease in u_p, the F_{Pd} and F_{Ph} gradually increased since the PSP was decelerated. As the PSP's velocity u_P converged, F_{Ph} gradually decreased. F_{Ph} took the maximum value of 0.011 μN at $t = 0.383$ sec. The maximum ratio of $|F_{Ph}|$ to $|F_{Pg}|$ was 3.5%. The PSP's acceleration was −4.0 mm/sec^2, and F_T was −0.002 μN, which is 0.6% of F_{Pg}. These forces were thus negligibly small.

— Place Fig. 7 here —

3.1.4. Estimation of the acoustic radiation force F_{Ba} acting on the ACOB

The acoustic radiation force acting on a bubble is commonly called the Bjerknes force, which can be divided into the primary Bjerknes force and the secondary Bjerknes force. To estimate the primary Bjerknes force, it is necessary to determine the absolute sound pressure amplitude acting on an ACOB. To calculate the secondary Bjerknes force (which is a bubble-bubble interaction), the three-dimensional distances among bubbles and their velocities in radial directions are necessary. Simultaneously measuring the absolute sound pressure and ACOBs' surface oscillations is impossible under the present circumstances. We therefore calculated the acoustic radiation force acting on the ACOB by subtracting the other forces

acting on the trapped PSP system from the total force:

$$F_{Ba} = F_T - \left(F_{Pb} + F_{Bb} + F_{Pd} + F_{Pv} + F_{Pp} + F_{Ph} + F_{Pa}\right). \quad (14)$$

F_{Ba} was calculated as 0.344 μN at $t = 0$ sec, and the time-averaged F_{Ba} and its standard deviation during the measurement period ($0 < t < 0.5$ sec) were 0.334 μN and 0.008 μN, respectively. When the PSP was stably trapped, F_{Ba} acted as a counterbalance to F_{Pg}.

The variations of the forces (F_{Pg}, F_{Pd}, F_{Pa}, and F_{Ba}) against the input power are plotted in Figure 8. F_{Pa} is a function of the stationary position and sound pressure amplitude. However, in the present study, we calculated F_{Pa} as a function of only the sound pressure amplitude due to the limited stationary position of the PSP and the simplification of the calculation. As a result, F_{Pa} decreased with the increase in P_{in}. During P_{in} from 1.0 W to 2.2 W, the PSP was stably trapped and u_{Pr} was small; the increment of F_{Ba} was almost equal to the increment of $|F_{Pa}|$. As shown in Figure 4, the PSP's position at $P_{in} = 0.79$ W and $P_{in} = 2.50$ W was unstable. At $P_{in} = 2.50$ W, the PSP gradually descended toward the SPAR during our measurement period. From these results, it is apparent that F_{Pg} and F_{Ba} dominantly acted on the PSP to hold it in the sound pressure field during the static state.

— Place Fig. 8 here —

3.2. The PSP's transitional motions against the amplitude change in the input power P_{in}

3.2.1. The PSP's motion under the transition state of input power P_{in}

In the visualization results, we observed a small amount of noise due to the camera's spatial resolution or the small fluctuation of the three-dimensional sound propagation. We removed this noise in light of the time-scale of the PSP's motion. The change patterns of the decrease (i.e., dP_{in}/dt) in P_{in} and the average PSP velocity $\overline{u_P}$ are listed in Table 1. Figure 9

shows the PSP's position in the z-direction during the amplitude change in P_{in}. Figure 9a shows the PSP's position in the z-direction versus time t, and Figure 9b shows P_{in} versus t (i.e., the patterns of the decrease in P_{in}).

By the gradual change in P_{in} (G1, G2, and G3 in Fig. 9), the PSP ascended gradually and inversely in response to the P_{in} change. After the PSP reached $z = 78$ mm, the PSP fluctuated moderately up and down. At this moment, P_{in} passed through approx. 1.3 W. After this fluctuation of the PSP's position, the PSP again ascended toward the LPAP. The $\overline{u_P}$ was 3.21 mm/sec (G1), 2.17 mm/sec (G2), and 1.31 mm/sec (G3), respectively. Finally, the PSP was trapped and stayed at the LPAR steadily. The stationary position of the PSP after the change of P_{in} corresponded to the stationary position under the static state of the corresponding input power. By increasing the change rate of P_{in}, the PSP reached the LPAR faster.

These results demonstrated that the PSP position and motion were strongly influenced by the sound pressure profile under the transition state of P_{in} and the stable sound pressure profile under the static state of P_{in} (which was set after the input power change). In addition, it is difficult to measure the sound pressure profile during the transition state of P_{in}, because hydrophones cannot be put in an experimental setup due to the change of an acoustic field.

On the other hand, under the step-like change of P_{in} ($dP_{in}/dt = -\infty$, S1, and S2 in Fig. 9), after the step-like change ($t > 1$), the PSP immediately sank. The $\overline{u_P}$ was −11.8 mm/sec (S1) and −12.4 mm/sec (S2), respectively. We next discuss this difference in $\overline{u_P}$ in light of the forces acting on the PSP and ACOB and the behavior of the PSP and ACOB.

— Place Table 1 here —

— Place Fig. 9 here —

3.2.2. The PSP's velocity u_P and its surrounding liquid velocity u_L under the transition state of input power P_{in}

The PSP's velocity u_P and its surrounding liquid velocity u_L at G2 are plotted in Figure 10. Figure 10a shows P_{in} versus t, and Figure 10b shows these velocities versus t. At G2, during the static state of P_{in} (t <1 sec), the PSP stayed at z = 74 mm, which was the midpoint of the LPAR and SPAR. By changing P_{in}, the PSP gradually ascended toward the LPAR and showed repeated acceleration and deceleration. The u_P was stable after it reached the LPAR. The u_L decreased gradually in association with the PSP's ascending motion. The u_L was smaller than the u_P throughout the measurement period. The fluctuation of u_P was large and periodical. When the PSP arrived at the LPAR, the fluctuation of u_P was drastic; it sharply increased and dropped. On the other hand, the fluctuation of u_L was small regardless of the PSP's position. From this point of view, the influence of u_L on u_P was negligible.

— Place Fig. 10 here —

The PSP's velocity u_P and its surrounding liquid velocity u_L at S2 are plotted in Figure 11. Figure 11a shows t versus P_{in}, and Figure 11b shows t versus these velocities. At S2, the PSP also stayed at z = 74 mm during the static state of P_{in} (t <1 sec). As shown in Figure 9a, the PSP sank in the step-like change of P_{in}, and the u_P rapidly decreased. The u_P converged at the PSP's terminal velocity $u_{P,t}$ of −13.3 mm/sec. The u_L was approx. −0.60 mm/s during the static state of P_{in} (t <1 sec). When the ultrasound irradiation was stopped through this step-like change, the u_L gradually increased. The u_L converged at −0.27 mm/sec when u_P converged. The acceleration of the surrounding liquid was 0.85 mm/sec^2. As a result, the influence of the surrounding liquid motion on the PSP's motion was small through the transition state of P_{in}.

— Place Fig. 11 here —

3.2.3. Force analysis under the gradual amplitude change of input power P_{in}

Figure 12 shows the results of the force analysis at G1. As mentioned above, $|u_L|$ was smaller than $|u_P|$. The contribution ratio of F_{Pp} to F_{Pg} was <1%, and F_{Bg} was also negligibly small. Before the gradual change of P_{in} (i.e., the static state of P_{in}), F_{Ba} acted as a counterbalance against F_{Pg} and F_{Pa}. By the gradual change of P_{in}, the relative velocity between u_P and u_L decreased due to the PSP's ascending motion. F_{Pa} gradually increased due to the decrease in P_{in}. F_{Pd} and F_{Ph} decreased when u_P increased. These forces acted as a brake against the PSP's ascent. As a result, the PSP moved downward. Conversely, as F_{Pd} and F_{Ph} increased, the PSP restarted an ascent toward the LPAR. The PSP's fluctuating motion around $z = 78$ mm was caused by the fluctuation of F_{Pd} and F_{Ph}. The reason for this fluctuation is discussed below.

— Place Fig. 12 here —

Figure 13 provides snapshots of the ACOBs pulling up the PSP toward the LPAR. As shown in Figure 13a, two ACOBs that are just restarting to move the PSP upward toward the LPAR are observed; one (ACOB1, marked with a red circle in Fig. 13) was held at the LPAR, and the other (ACOB2, marked with a yellow circle in Fig. 13) is attached to the PSP's surface. As the PSP was approaching the LPAR (Fig. 13b–f), ACOB1 turned into ACOB2. As shown in Figure 13g, ACOB1 and ACOB2 coalesced. The coalesced ACOB led the PSP toward the LPAR (Fig. 13g–j). This result indicated that the ACOBs interacted with each other.

The influence of the secondary Bjerknes force on the PSP motion was increased when the PSP was positioned close to the LPAR. Therefore, the increment of F_{Ba} resulted from the

secondary Bjerknes force, and this caused the fluctuation of F_{Pd} and F_{Ph}. The $|u_P|$ under the gradual change in P_{in} was smaller than the $|u_P|$ under the step-like change in P_{in}. The fluctuations of the forces F_T, F_{Pd}, F_{Ph}, and F_{Pv} were small. Throughout the gradual change in P_{in}, the force balance was maintained mostly between F_{Ba} and F_{Pg}.

— Place Fig. 13 here —

3.2.4. Force analysis under the step-like amplitude change of input power P_{in}

Figure 14 shows the results of the force analysis at S1. Before the step-like change of P_{in} (t <1 sec), F_{Ba} balanced with F_{Pa} and F_{Pg}. The other forces were negligibly small. In this situation, the amplitude of ultrasound irradiation was attenuated, and F_{Pa} was enlarged. As the PSP's downward velocity u_P increased, F_{Ph} was upwardly increased. In addition, F_{Pd} was also enlarged due to the fast sedimentation speed of the PSP. F_T and F_{Pv} at t = 1.0 sec were estimated as −0.084 μN and 0.040 μN, respectively. F_{Pp} was almost zero throughout the step-like change of P_{in} due to the small u_L.

Our understanding of the entire picture of the forces acting on the PSP and ACOBs takes precedence over the precise profile of the forces in this study. We adopted an appropriate smoothing process that gave us stable calculation results. Consequently, in the step-like change of P_{in}, the sharpness of the decline of F_{Ba} was insufficient.

— Place Fig. 14 here —

Figure 15 shows the results of the force analysis at S2. After the step-like change of P_{in}, F_{Pa} became zero. In the same way as in the S1 condition, F_{Pd} and F_{Ph} were increased because the PSP rapidly sank. F_{Pp} was almost zero throughout this step-like change due to the small u_L. The influence of the liquid motion on the particle motion was negligibly small. Conversely, F_{Ba} weakened and converged on zero.

Under the step-like change of P_{in}, the dominant forces were switched from F_{Pg}, F_{Pa}, and F_{Ba} (before the step-like change) to F_{Pg}, F_{Pd}, F_{Ph}, and F_{Ba} (after the step-like change).

— Place Fig. 15 here —

3.2.5. Consideration of the influence of the ACOB's motion on the PSP's motion

Although the amplitude of P_{in} under the gradual amplitude changes (G1, G2, and G3) was the same as that under the step-like change (S1), the PSP's motion differed notably with the patterns of the change of P_{in}. F_{Ba} is thought to influence the PSP's motion. To elucidate the change in the acoustic radiation force acting on ACOB, we visualized the ACOB's surface oscillation under the gradual and step-like amplitude changes of P_{in}.

The ACOB diameter during the transition state of P_{in} at S1 is plotted in Figure 16. During the static state (t <0.5 sec), the ACOB oscillated in synchronization with the irradiation frequency, and the time-averaged ACOB diameter before the input power change was estimated as 72.3 μm. By the step-like change of P_{in}, F_{Ba} rapidly attenuated, and the bubble oscillation was rapidly attenuated too. The time-averaged ACOB diameter after the change of P_{in} at S1 rapidly decreased to 29.7 μm, and the amplitude of the diameter's oscillation changed periodically. The small amplitude of this diameter's oscillation resulted from the decrement of F_{Ba} in light of the equation of the primary Bjerknes force.

— Place Fig. 16 here —

Figure 17 shows the ACOB's motion after the step-like change of P_{in} under the S2 condition. At S2, since the ultrasound was not irradiated into the vessel, the ACOB stopped its surface oscillation very quickly after the step-like change (probably after a very short time

lag resulting from the remaining motion of the surrounding water). The time-averaged ACOB diameter after the change of P_{in} at S2 was estimated as 30.8 μm, which was very similar to that at S1; however, the amplitude of the diameter oscillation at S2 was much smaller than that at S1. Rather, this oscillation should be considered to be brought about by the spatial resolution (6.25 μm/pixel). These results comprise good evidence that this ACOB at S2 was a remaining bubble that originated from the acoustic cavitation.

— Place Fig. 17 here —

The ACOB's diameter at G1 is plotted in Figure 18. By the gradual change of P_{in}, the sound pressure amplitude near the particle was decreased. The ACOB kept its surface oscillation after the gradual change of P_{in}. The ACOB diameter was slightly increased with the PSP's ascent. In this case, although the amplitude of P_{in} was decreased, the PSP moved toward the LPAR. We speculate that the decrease of the sound pressure amplitude near the PSP at the gradual change was smaller than that at the step-like amplitude change. In addition, the ACOB's diameter grew with the PSP ascent. F_{Ba} was calculated by the multiplication of the ACOB volume and sound pressure amplitude (i.e., the primary Bjerknes force). The increment of the ACOB's volume compensated for the decrement of the sound pressure amplitude. Thus, F_{Ba} did not decrease under the gradual amplitude change of P_{in}. This result well accorded with the force analysis results. The ACOB's surface oscillation influenced the PSP's motion; i.e., the PSP's motion was strongly affected by F_{Ba}.

— Place Fig. 18 here —

3.3. Consideration of the influence of the particle size on the particle classification

3.3.1. Consideration of the influence of the particle size and forces

In order to classify particles by their diameters on the basis of our new knowledge, we needed to consider the relationship between the particle size and forces acting on the particle held in the sound pressure field. The ratios of the forces to F_{Pg} are shown in Figure 19. The ratios increased with the decrease in the particle's diameter. When the ACOB diameter was 100 μm, the ratio of F_{Bg} to F_{Pg} at the 400-μm-dia. particle was 16 times as large as that at the 1000-μm-dia. particle. In light of F_{Pd}, when a particle sank (in the present study, the liquid motion velocity was negligibly small), F_{Pd} acted upwardly. With the increment of the particle diameter, the contribution ratio of F_{Pd} to F_{Pg} declined. Since the settling velocity of larger-diameter particles was larger than that of smaller-diameter particles, naturally the larger-diameter particles sank faster than the smaller-diameter particles.

We considered a situation in a particle classification process. In this process, the number of particles was large, and the number of ACOBs was also large. We dealt with multiple ACOBs when particles were classified according to their diameters. We hypothesized that the ACOBs' diameters are the same if the properties of ultrasound irradiation are the same; thus F_{Bg} was the same. F_{Ba} acted as though it was holding particles at the LPAR. With the gradual amplitude change of P_{in}, the forces acting to hold the particles at the LPAR were attenuated. This implied that the larger-diameter particles started sinking before the smaller-diameter particles sank under the gradual decrement of P_{in}. By decreasing P_{in} further (i.e., decreasing the sound pressure amplitude further), the smaller-diameter particles started sinking because of the decrease of F_{Ba}. A gradual amplitude change of P_{in} can make use of the effects of both F_{Pd} and F_{Ba}. Thus, a gradual amplitude change of P_{in} is better and more useful than a step-like amplitude change of P_{in} when using our particle classification technique.

— Place Fig. 19 here —

3.3.2. Demonstration of the particle classification under the step-like amplitude change of input power P_{in}

We conducted the particle size classification under the step-like/gradual amplitude change of P_{in}. Figure 20 shows a typical visualization result and its amplitude change of P_{in} during the transit period in the step-like amplitude change. As shown in Figure 20a, the SFPS composed of the larger-diameter PSPs and smaller-diameter PSPs was held in the upper LPAR. By the step-like amplitude change of P_{in}, F_{Ba} decreased instantaneously. The acoustic radiation force acting on the ACOB F_{Ba} and the acoustic radiation force acting on the PSP F_{Pa} were weakened. Immediately, the SFPS's spherical shape crumbled. Both larger-diameter and smaller-diameter PSPs sank and started dispersing in the horizontal and vertical directions (Fig. 20b). The PSPs positioned at the bottom edge of the SFPS sank vertically due to the weak interaction between the PSPs. The other PSPs were horizontally spread due to (1) the strong interaction between the PSPs themselves, (2) the interaction between the preceding-sinking particles and the surrounding liquid motion, and (3) the sudden attenuation of the acoustic radiation force acting on the ACOBs.

The extent of the dispersion of the larger particles was similar to that of the smaller particles (Fig. 20c). At the moment when the input power was restored, the larger- and smaller-diameter PSPs were dispersed more widely in the vessel (Fig. 20d). The PSPs dispersed near the upper LPAR were re-flocculated at the upper LPAR since F_{Ba} and F_{Pa} were increased (Fig. 20e). The other PSPs, which are positioned in the lower region in Figure 20e, were sparsely dispersed in the lower LPAR. As shown in Figure 20f, the SFPS had reverted to its former state of flocculation. Thus, a step-like amplitude change is not suitable for a particle separation/classification.

— Place Fig. 20 here —

3.3.3. Demonstration of the particle classification under the gradual amplitude change of input power P_{in}

A typical visualization result of the particle classification process under the gradual amplitude change of P_{in} is shown in Figure 21. The SFPS was trapped at the upper LPAR, which was the same result as that of the step-like condition. With the gradual decrease of P_{in}, F_{Ba} was slightly attenuated. The trapped SFPS gradually sank while keeping its shape (Fig. 21b); this state is different from that shown in Figure 20b. As P_{in} decreased further, the SFPS was not able to keep its shape (Fig. 21c); however, the dispersion area of the PSPs was smaller and denser than that shown in Figure 20c, due to the gradual-change effects of the acoustic radiation force acting on the ACOBs.

The larger-diameter PSPs started sinking before the smaller-diameter PSPs sank, since the contribution ratio of F_{Ba} to F_{Pg} of the large-diameter particles was small. The horizontal extent of PSPs under the gradual decrease in P_{in} was narrower than that under the step-like decrease. As shown in Figure 21d, the smaller-diameter PSPs were still dispersed in the upper region, whereas the larger-diameter PSPs were dispersed in the lower region of the vessel. With the gradual restoration of P_{in}, the F_{Ba} gradually increased. The PSPs started forming SFPSs at both the lower LPAR and upper LPAR (Fig. 21e). As P_{in} increased further, two SFPSs were trapped (Fig. 21f); interestingly, one SFPS (upper side in Fig. 21f) was composed of smaller-diameter PSPs, and the other SFPS (lower side in Fig. 21f) was composed of larger-diameter PSPs. This slow flocculation process was thus better for avoiding the unhelpful flocculation of the PSPs under the step-like condition.

Compared with the step-like change of P_{in}, the gradual amplitude change of P_{in} is

optimal for our particle size classification technique. We concluded that a lower decreasing rate of P_{in} provided a highly efficient particle classification in consideration of the effects of subtly breaking the balance among the forces and recovering the balance.

— Place Fig. 21 here —

4. Conclusions

We investigated the forces acting on a single particle trapped in water by a sound pressure field. Since the particle was trapped in water by the acoustic effects of the acoustic cavitation-oriented bubble (ACOB), we focused on nine types of forces. Under the static state of the acoustic field, the trapping position was changed by varying the input power to the ultrasound transducer. To hold the particle in the sound pressure field, the acoustic radiation force acting on the ACOB, F_{Ba}, was counterbalanced by gravitational and buoyancy forces acting on the PSP, F_{Pg}, and the acoustic radiation force acting on the PSP, F_{Pa}.

We examined two types of amplitude change of the input power in order to investigate the influence of the forces on the particle motion. Under the step-like amplitude change, the particle immediately sank due to the very marked decrease in F_{Ba}. The force balance was shifted from "F_{Pg} and F_{Pa} versus F_{Ba}" to "F_{Pg} versus a drag force acting on a PSP F_{Pd} and a Basset history force acting on the PSP F_{Ph}". On the other hand, under the gradual change of the input power P_{in}, the PSP was moved toward the LPAR by the amplitude change (i.e., mainly the change in the effects of the acoustic radiation forces). The ACOB's diameter increased with the particle's ascent. The force balance was not changed by the gradual amplitude change; F_{Ba} and F_{Pg} were dominant, and balanced. The PSP's motion was strongly affected by F_{Ba}.

We considered the influence of the particle diameter on the particle motion. By

decreasing the particle diameter, the ratios of the forces to F_{Pg} were increased. We conducted the particle size classification under the two types of amplitude change of P_{in}. Under the step-like amplitude change, the spherically flocculated particle swarm (SFPS) was re-flocculated at the same position in the vessel. Under the gradual amplitude change, the larger-diameter particles started sinking before the smaller-diameter ones did. The smaller-diameter particles were spherically re-flocculated at the upper region in the vessel, and the larger-diameter particles were spherically flocculated at the lower region in the vessel. These results demonstrate an innovative particle separation and classification technology using low-frequency ultrasound irradiation in liquid and the control of the amplitude change of the input power P_{in}. Our present findings revealed that the gradual amplitude change produces a highly efficient classification of particles based on their diameters.

Acknowledgements

This study was promoted and financially supported by Category 'A' of the Grants-in-Aid for Scientific Research, Japan Society for the Promotion of Science (JSPS). We thank the JSPS for its help. We declare no conflicts of interest.

Nomenclature

Symbol

c_{gP} : gravity center of a PSP, mm

c_L : sound speed in water, m/sec

C_D : drag coefficient (−)

C_V : virtual mass coefficient (−)

D_P : diameter of a PSP, mm

D_B : equivalent diameter of an ACOB, μm

E : average density of acoustical energy, J/m^3

f : ultrasound irradiation frequency, kHz

F_{Ba} : acoustic radiation force acting on an ACOB, μN

F_{Bg} : buoyancy force acting on an ACOB, μN

F_{Pa} : acoustic radiation force acting on a PSP, μN

F_{Pd} : drag force acting on a PSP, μN

F_{Pg} : gravitational and buoyancy force acting on a PSP, μN

F_{Ph} : Basset history force acting on a PSP, μN

F_{Pp} : pressure gradient force acting on a PSP, μN

F_{Pv} : Virtual mass force acting on a PSP, μN

F_T : total force, μN

g : gravitational acceleration, m/sec^2

k : wave number, 1/m

p : sound pressure, kPa

P_{in} : input power to the ultrasound transducer, W

S_P : PSP's cross-sectional area, mm^2

t : time, sec

u_L : PSP's surrounding liquid-phase velocity, mm/sec

u_P : PSP's velocity, mm/sec

u_{Pr} : relative velocity between u_P and u_L, mm/sec

V_B : volume of an ACOB, mm^3

V_P : volume of a PSP, mm^3

Greek letters

λ : wavelength, mm

μ : viscosity, Pa•sec

ρ_L : density of a liquid phase, kg/m^3

ρ_P : density of a PSP, kg/m^3

References

Clift, R., Grace, J.R., Wever, M.E., 1978. Bubbles, Drops, and Particles. Academic Press, New York.

Gor'kov, L.P., 1962. On the forces acting on a small particle in an acoustical field in an ideal fluid. Sov. Phys. Dokl., 6, 773–775.

Kozuka, T., Yasui, K., Tuziuti, T., Towata, A., Iida, Y., 2007. Noncontact acoustic manipulation in air. Jpn. J. Appl. Phys., 49, 4948-4950.

Matula, T.J., Cordry, S.M., Roy, R.A., Crum, L.A., 1997. Bjerknes force and bubble levitation under single-bubble sonoluminescence conditions. J. Acoust. Soc. Am., 102 (3), 1522-1527.

Mitome, H., 2001, Micro bubble and sonoluminescence. Jpn. J. Appl. Phys. 40, 3484-3487.

Mizushima, Y., Nagami, Y., Nakamura, Y., Saito, T., 2013. Interaction between acoustic cavitation bubbles and dispersed particles in a kHz-order-ultrasound irradiated water. Chem. Eng. Sci., 93, 395-400.

Muramatsu, H., Yanai, S., Mizushima, Y., Saito, T., 2015. A novel particle separation technique using 20-kHz-ultrasound irradiation in water. J. Phys.: Conference Series, 656, 012117.

Muramatsu, H., Saito. T, 2017. The relationship between bubble motion and particle flocculation pattern under 20-kHz-ultrasound radiation in water. Chem. Eng. Sci., 170, 195-203.

Muramatsu, H., Saito, T., 2018. An innovative unit operation of particle separation/classification by irradiating low-frequency ultrasound into water. AIChE J., 64, 1564-1572.

Ochiai, Y., Hoshi, T., Rekimoto, J., 2014. Three-dimensional mid-air acoustic manipulation by ultrasonic phased arrays. PLoS One, 9, e97590.

Parajuli, D., Takahashi, A., Tanaka, H., Ogawa, H., Hakuta, Y., Yoshino, K., Funahashi, T., Yamaguchi, M., Osada, M., Kawamoto, T., 2016. Application of Prussian blue nanoparticles for the radioactive Cs decontamination in Fukushima region. J. Environ. Radioact., 151, 233-237.

Saito, T., Miyamoto, Y., Sakakibara, K., Yamada, M., 2010. A study of surfactant effects on the liquid-phase motion around a zigzagging-ascent bubble using a recursive cross-correlation PIV. Chem. Eng. J., 158, 39-50.

Woodside, S.M., Piret J.M., 1997. Measurement of ultrasonic forces for particle-liquid separations. AIChE J., 43 (7), 1727-1736.

Yanai, S., Saito, T., 2017. A novel particle classification technique arising from acoustic-cavitation-oriented bubbles (ACOBs) under kHz-band ultrasonic irradiation in water. Advances in Intelligent Systems and Computing, 519, 183-187. doi: https://doi.org/10.1007/978-3-319-46490-9_26.

Figure Captions

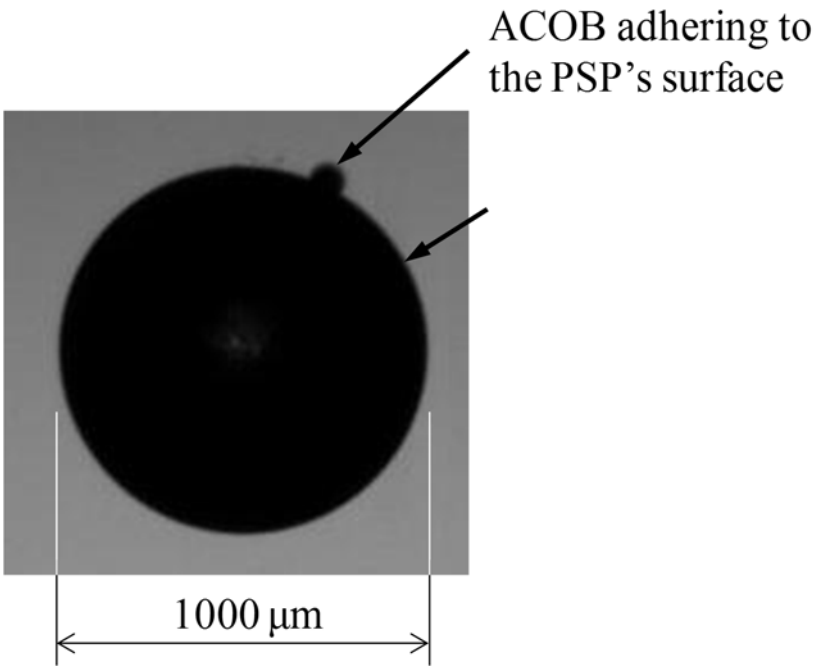

Fig. 1. A typical snapshot of a trapped PSP in a sound pressure field.

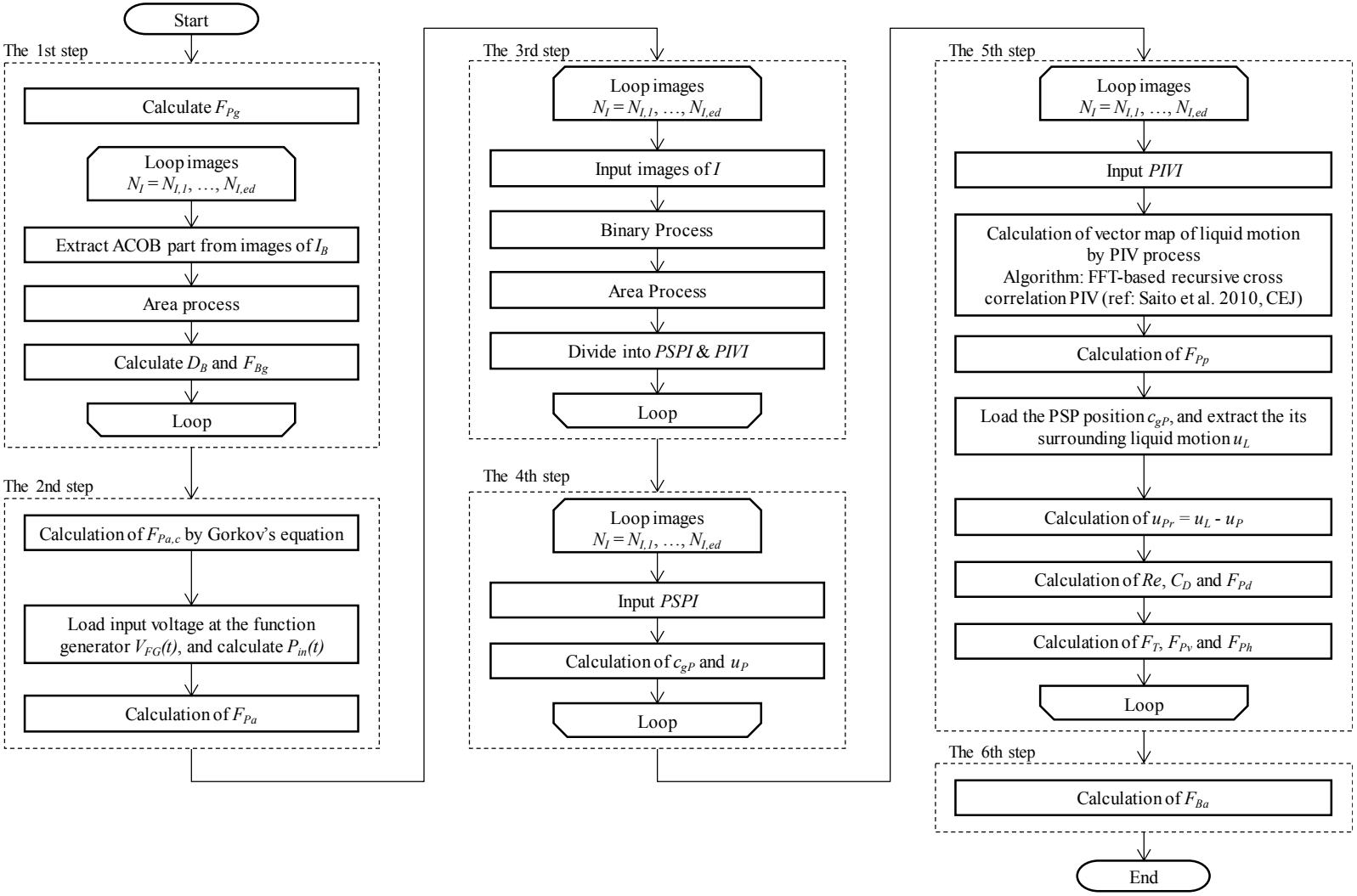

1 **Fig. 2.** The force analysis procedure.

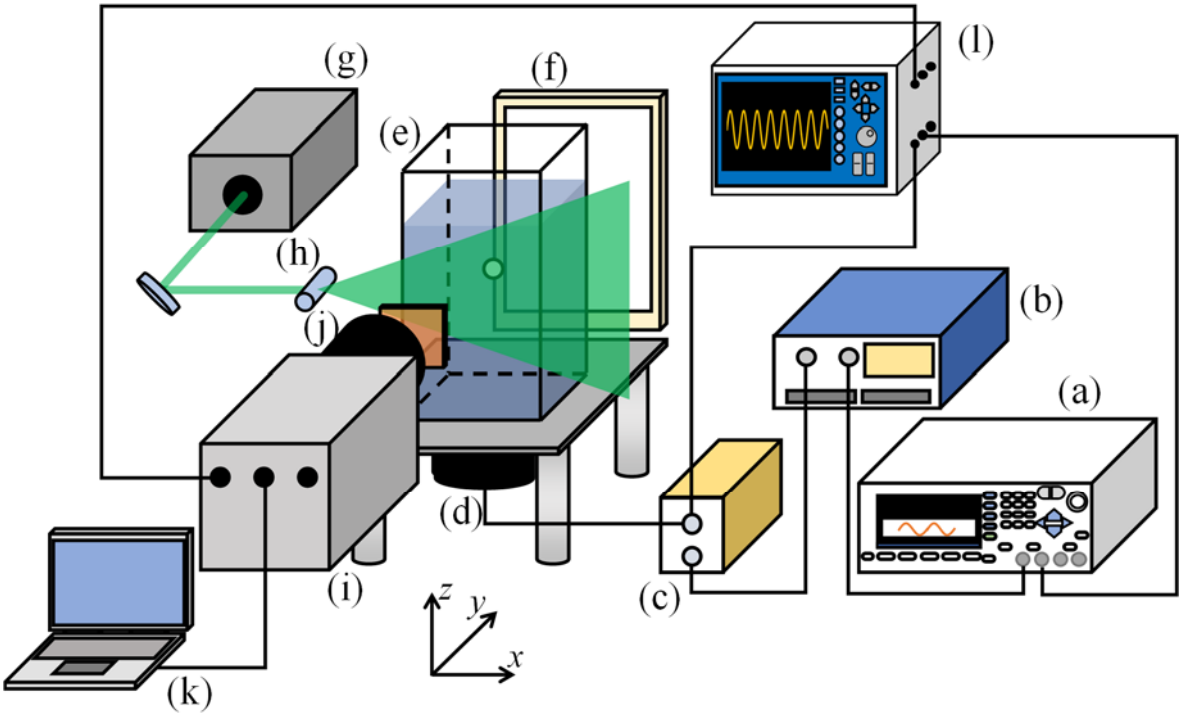

Fig. 3. Schematic of our experimental setup for the simultaneous visualization of the PSP's motion and the motion of its surrounding liquid. **a:** Function generator. **b:** Amplifier. **c:** Impedance matching circuit. **d:** Transducer. **e:** Acrylic vessel. **f:** LED light. **g:** YAG-laser. **h:** Rod lens. **i:** High-speed camera. **j:** Sharp-cut filter. **k:** PC. **l:** High-speed A/D converter.

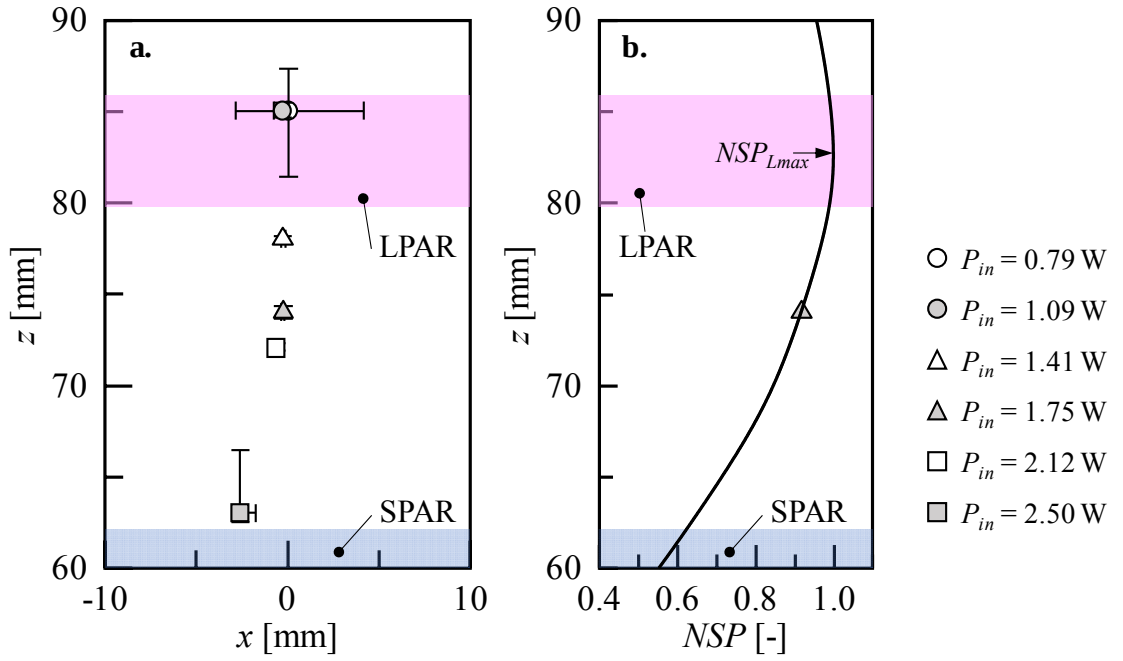

1

2 **Fig. 4.** The PSP's stationary position under a static state of the input power P_{in}. **a:** PSP's

3 stationary position. **b:** Normalized sound pressure profile on the center axis of the vessel.

4

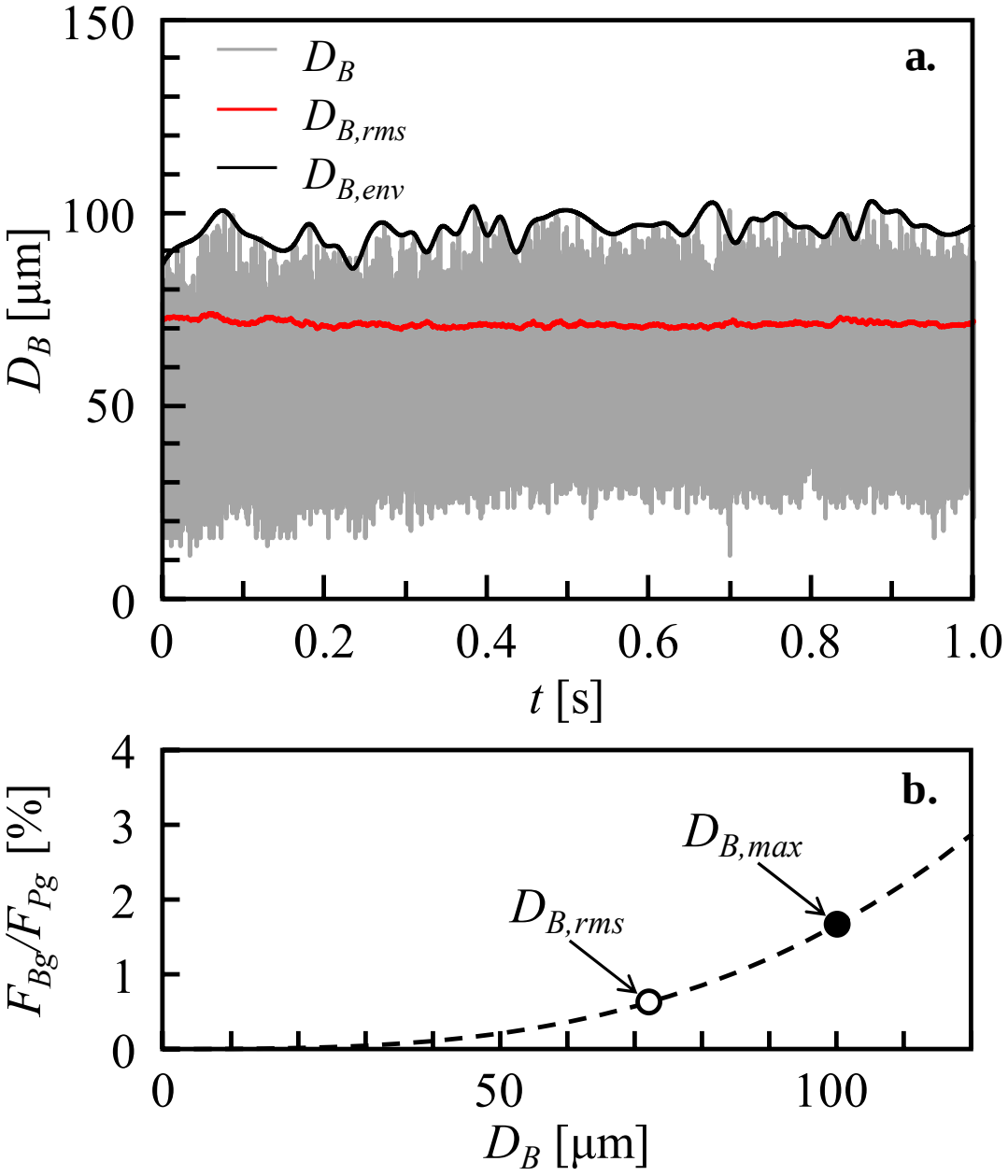

Fig. 5. The dynamics of an ACOB adhering to the trapped PSP's surface under a static state of the input power P_{in} (1.75 W). **a:** Time series of the ACOB's diameter. **b:** The ratio of the ACOB's buoyancy to the PSP's buoyancy.

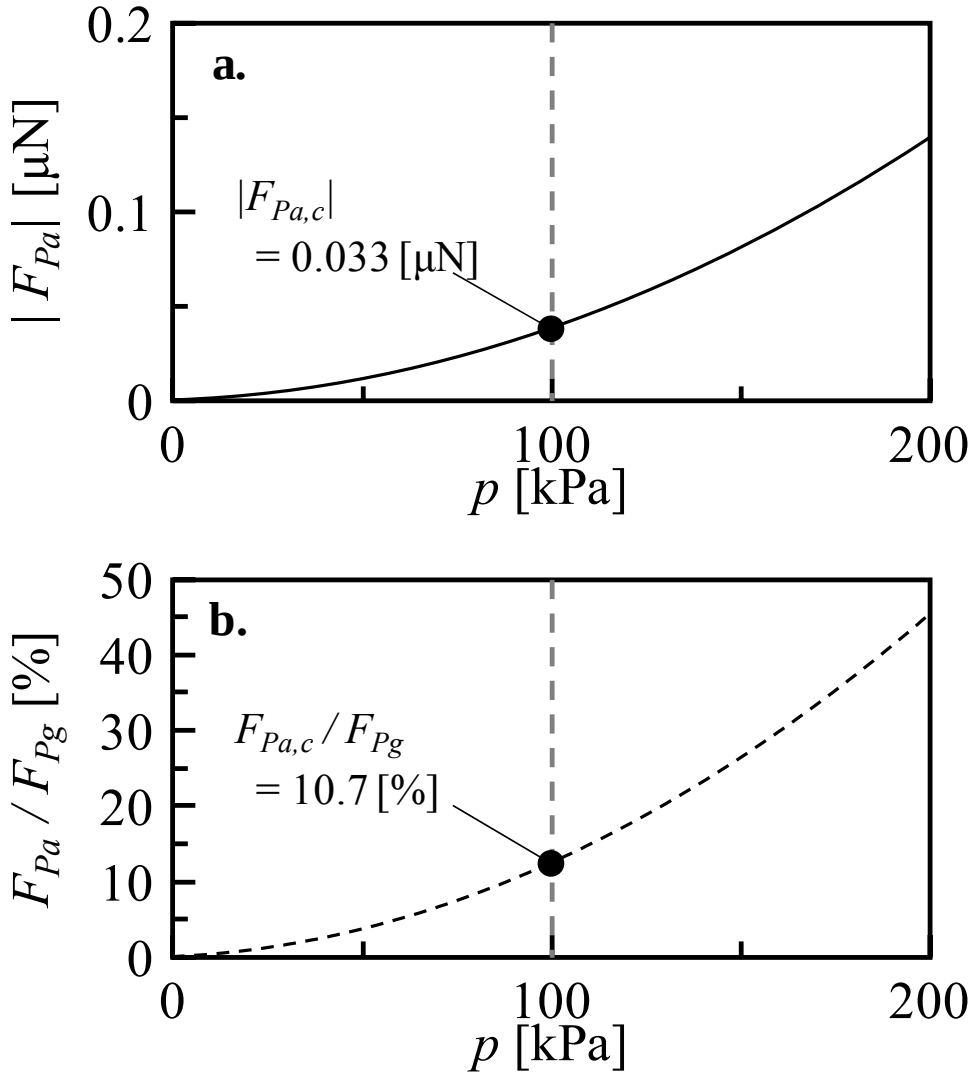

Fig. 6. Numerical results of the acoustic radiation force acting on the PSP. **a:** The relationship between the sound pressure amplitude and force. **b:** The ratio of the acoustic radiation force acting on the PSP to the PSP's buoyancy.

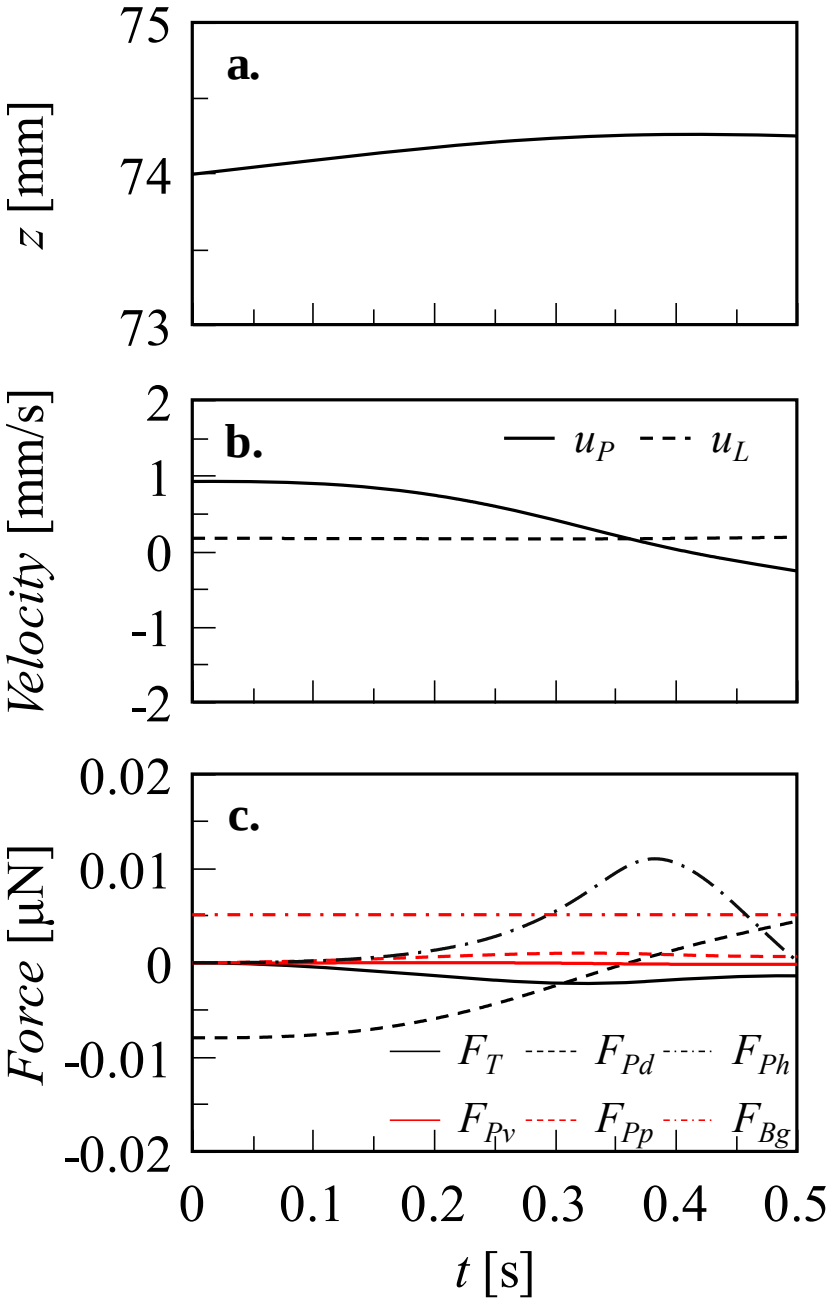

Fig. 7. Results of the force analysis under the static state of the input power (P_{in} = 1.75 W). **a:** Time-series z-position of the PSP. **b:** Time series of velocities of the PSP motion and its surrounding liquid motion. **c:** Time series of forces (F_T, F_{Bg}, F_{Pd}, F_{Pv}, F_{Pp}, and F_{Ph}).

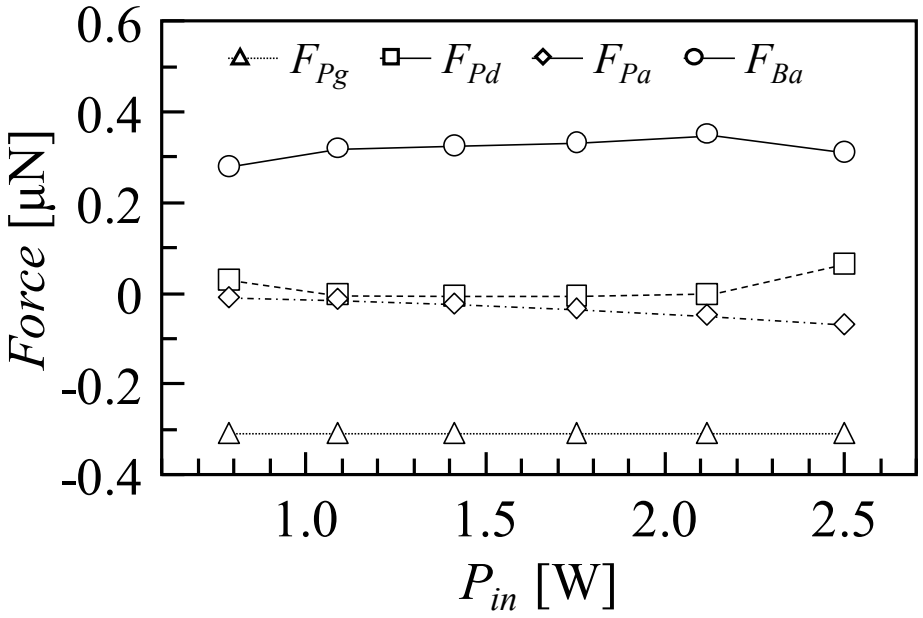

Fig. 8. The variation of the forces (F_{Pg}, F_{Pd}, F_{Pa}, and F_{Ba}) in the input power P_{in}.

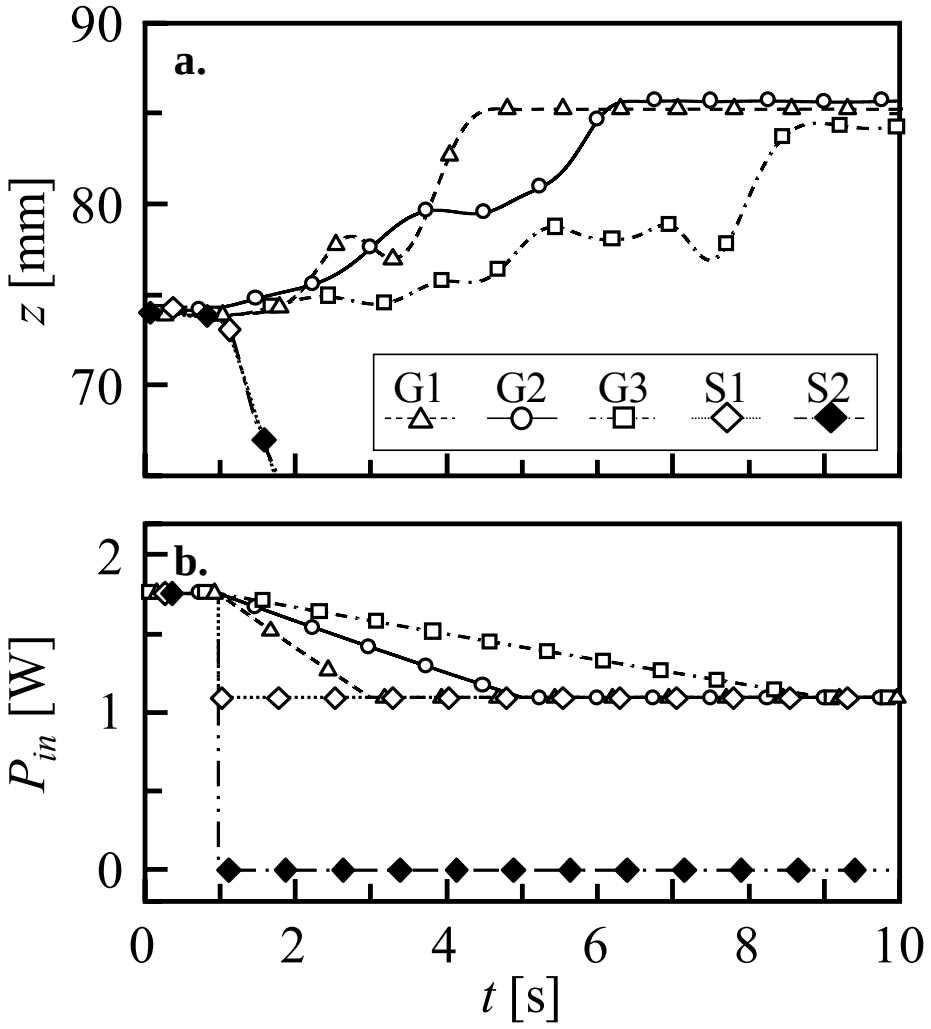

Fig. 9. The PSP's motion in the *z*-direction under a transition state of P_{in}. **a:** The PSP's motion in the *z*-direction. **b:** Amplitude change of input power P_{in}.

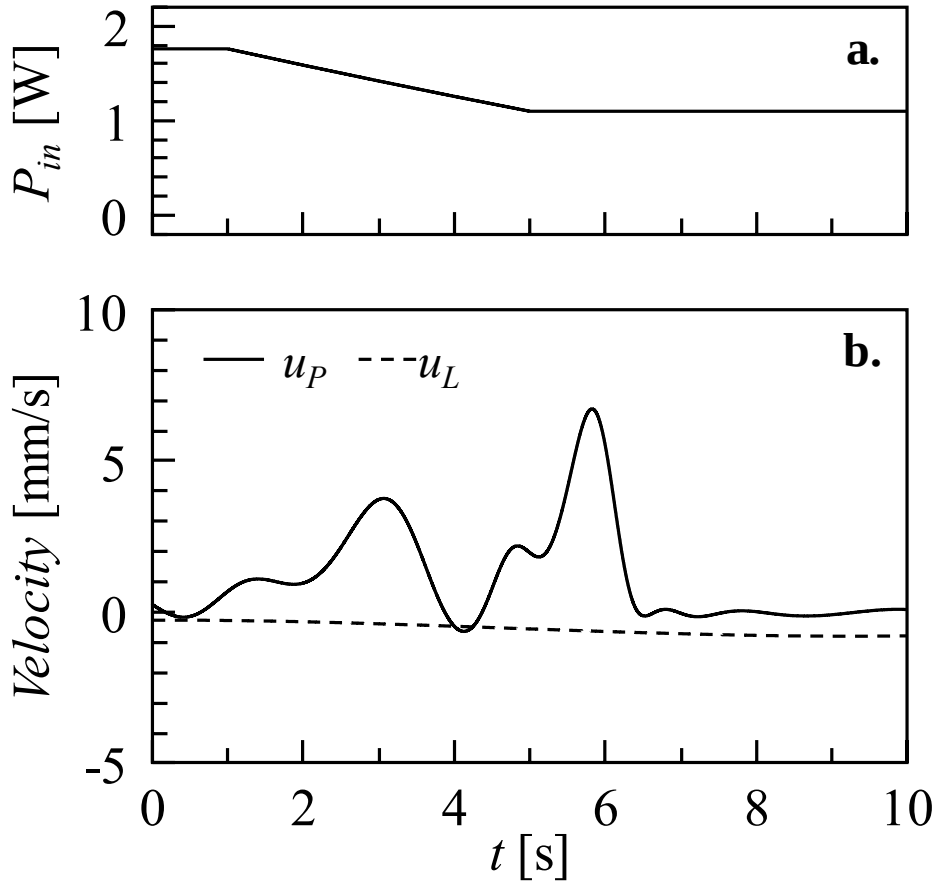

Fig. 10. Velocities of the PSP and its surrounding liquid during the transition state of the amplitude change of P_{in} at G1. **a:** Input power P_{in}. **b:** Velocities.

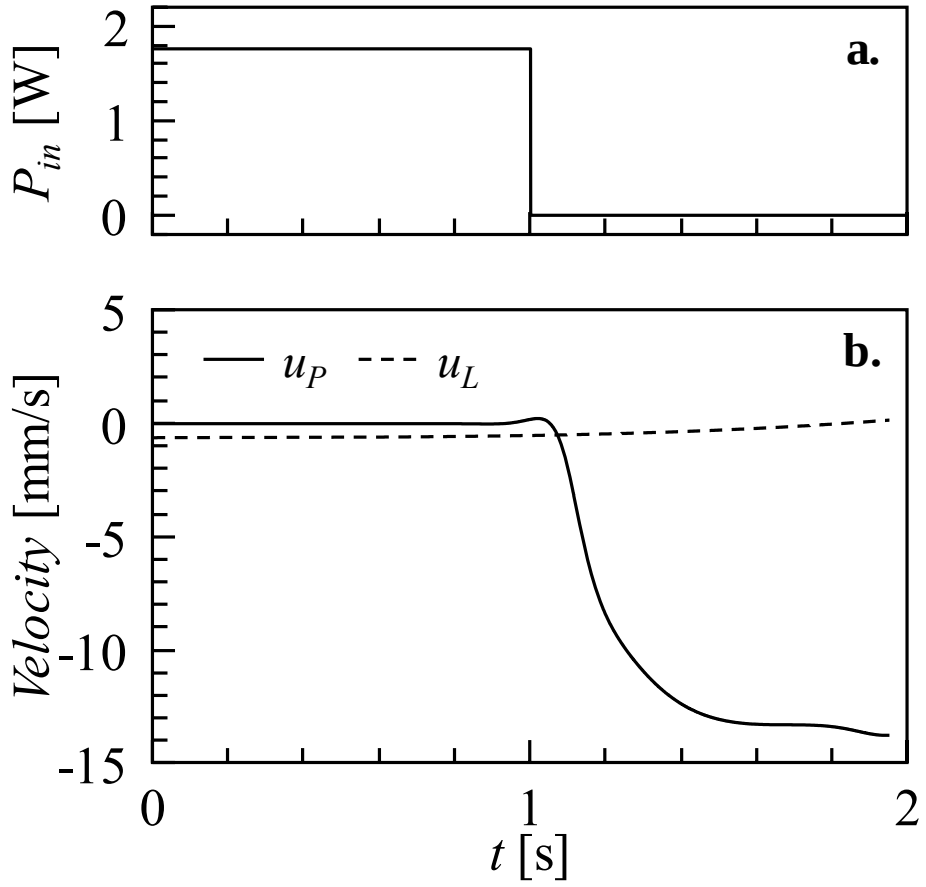

Fig. 11. Velocities of the PSP and its surrounding liquid during the transition state of the amplitude change of P_{in} at S2. **a:** Input power P_{in}. **b:** Velocities.

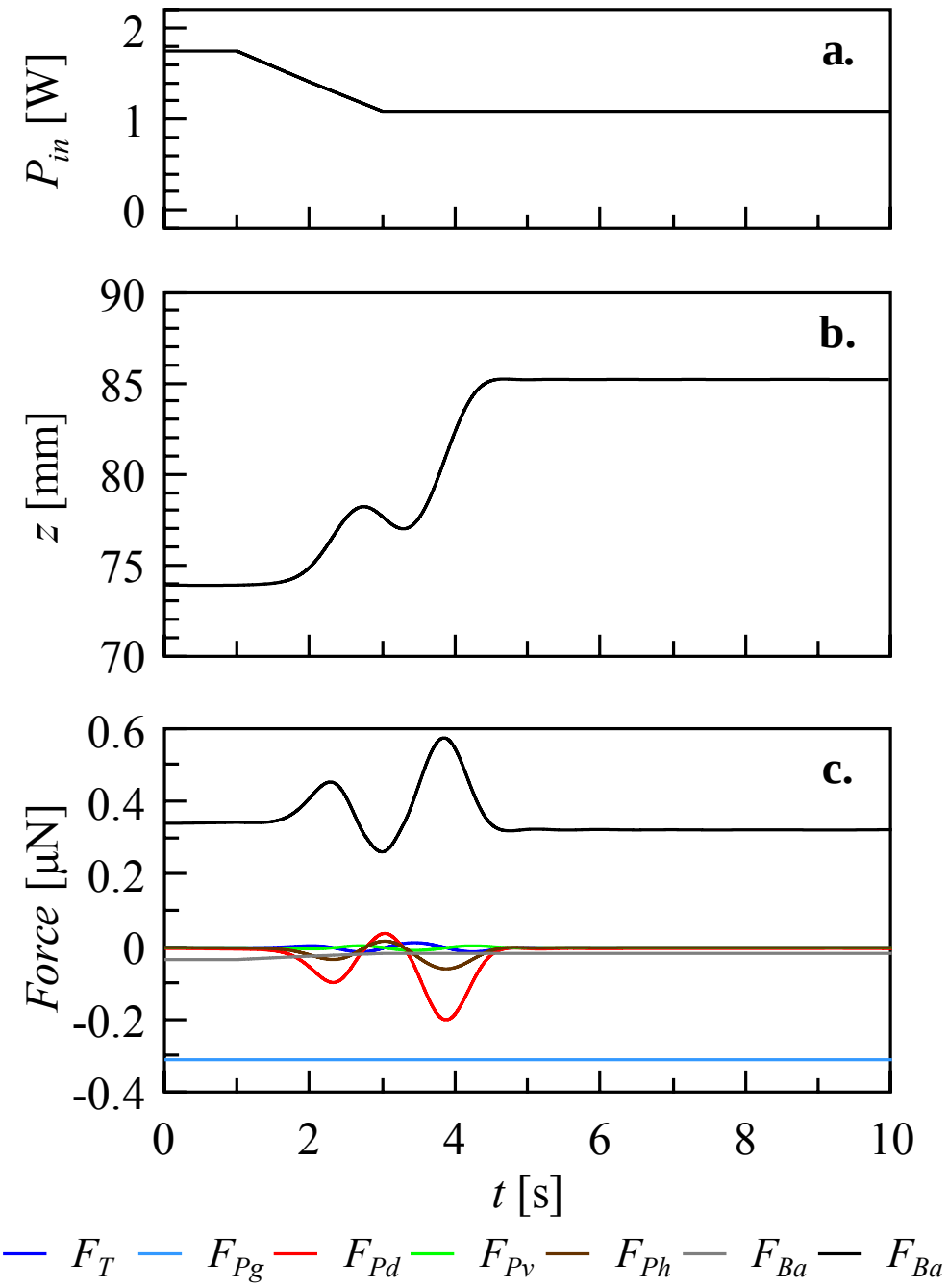

Fig. 12. Force analysis during the transition state of the amplitude change of P_{in} at condition G1. **a:** Input power P_{in}. **b:** Particle position in z. **c:** Forces.

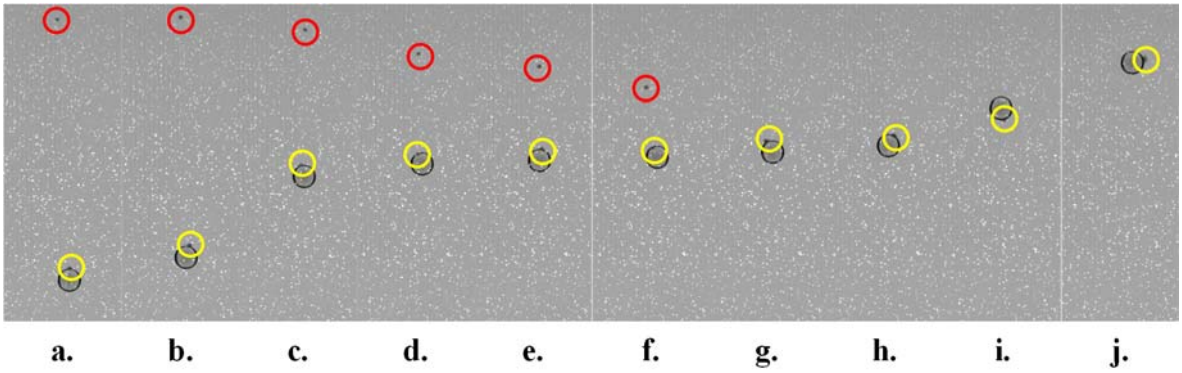

Fig. 13. Time series snapshots while the PSP was pulled up to the LPAR. **a:** $t = 3.500$ sec. **b:** $t = 3.600$ sec. **c:** $t = 3.900$ sec. **d:** $t = 3.950$ sec. **e:** $t = 3.963$ sec. **f:** $t = 3.975$ sec. **g:** $t = 3.988$ sec. **h:** $t = 4.000$ sec. **i:** $t = 4.100$ sec. **j:** $t = 4.400$ sec. a: The PSP restarted moving upward toward the LPAR. b–f: The PSP moved toward the LPAR. The ACOB held at the LPAR (*red circle*) gradually moved downward. g: The ACOB that adhered to the PSP surface (*yellow circle*) and the other ACOB (*marked red circle*) collapsed. h–j: The ACOB and PSP moved upward and became trapped at the LPAR.

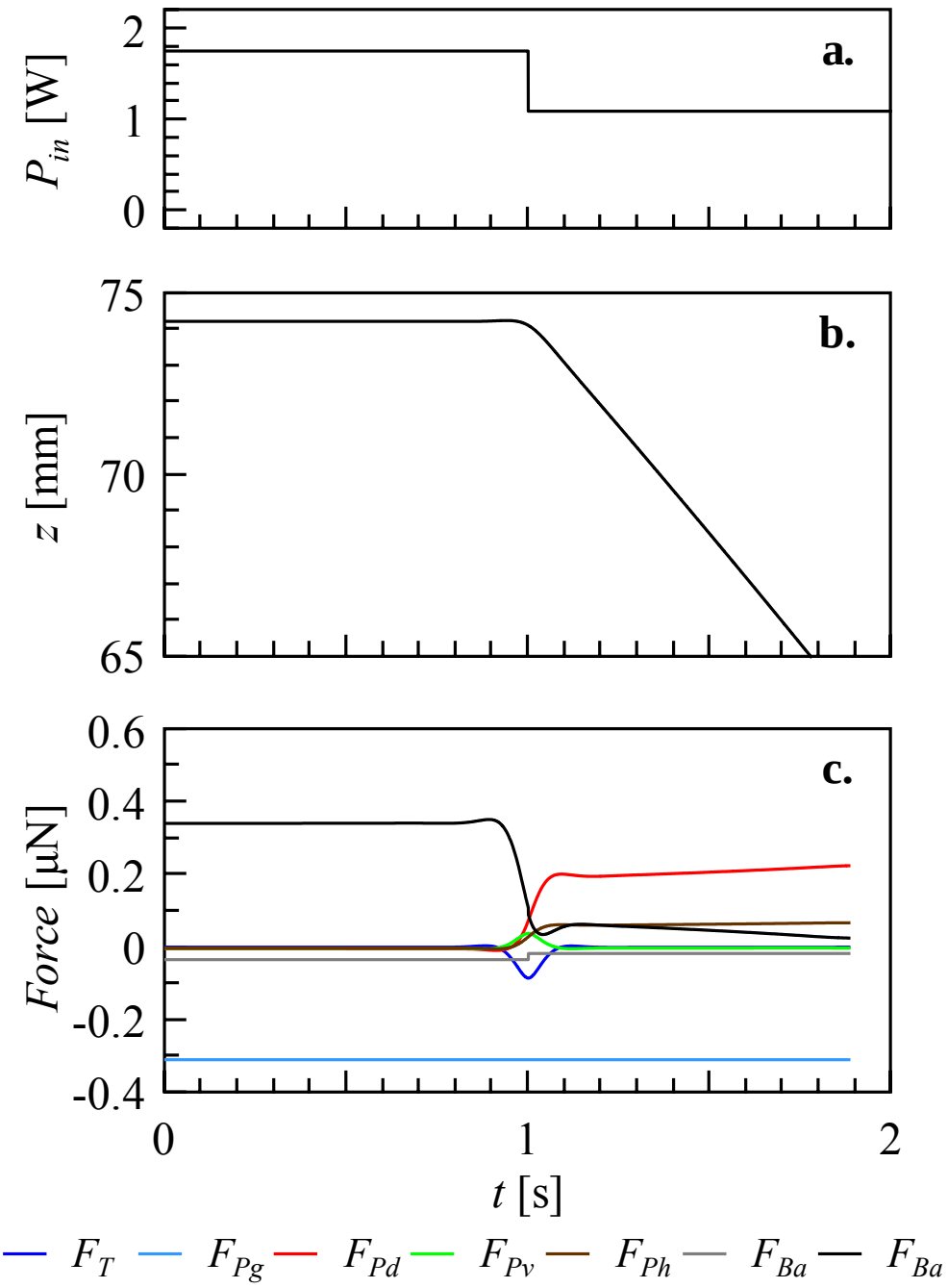

Fig. 14. Force analysis during the transition state of amplitude change of P_{in} at condition S1.

a: Input power P_{in}. **b:** Particle position in z. **c:** Forces.

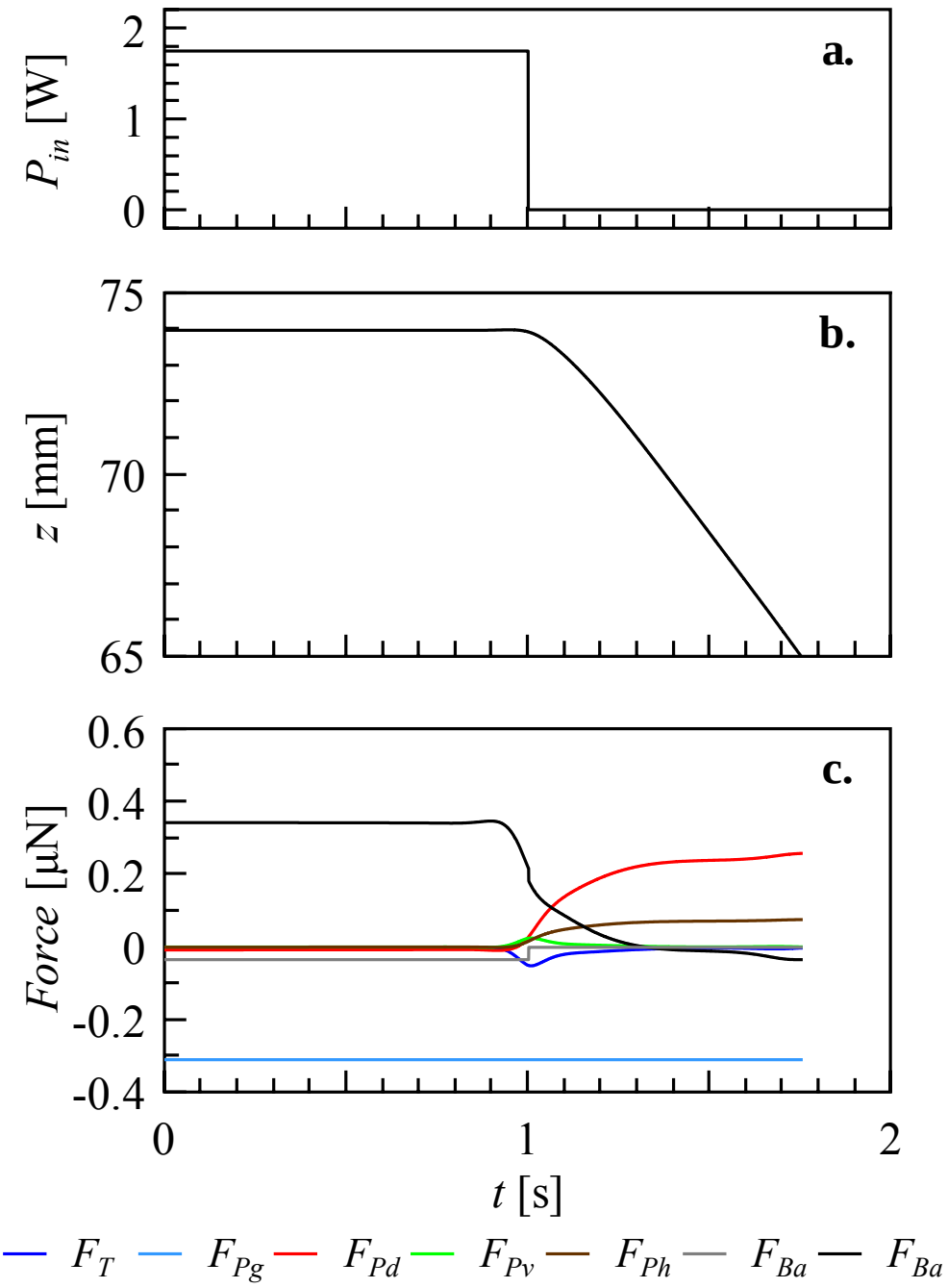

Fig. 15. Force analysis during the transition state of amplitude change of P_{in} at condition S2.

a: Input power P_{in}. **b:** Particle position in z. **c:** Forces.

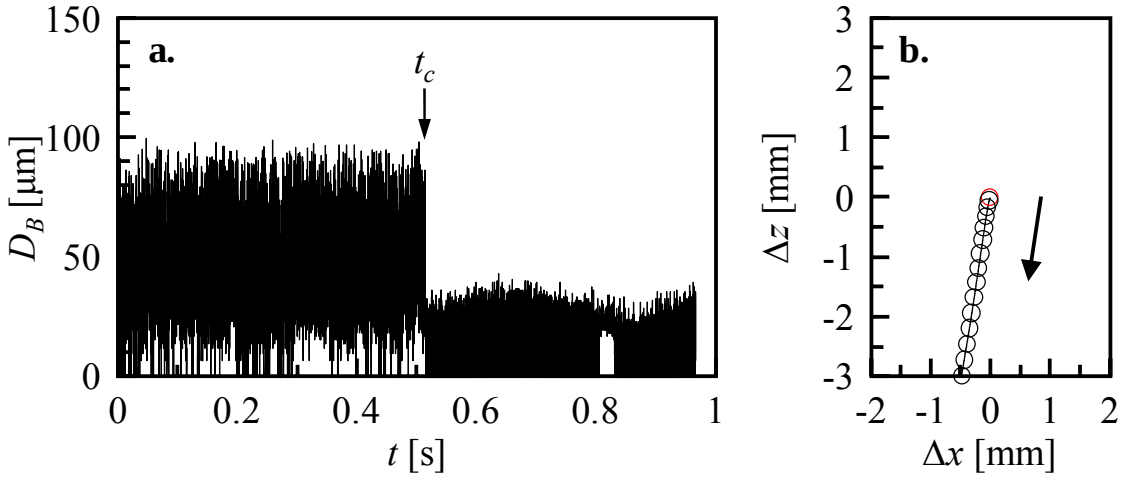

Fig. 16. Visualization results of the PSP's position change and the ACOB's diameter under S1. **a:** The ACOB's diameter. **b:** The PSP's position change.

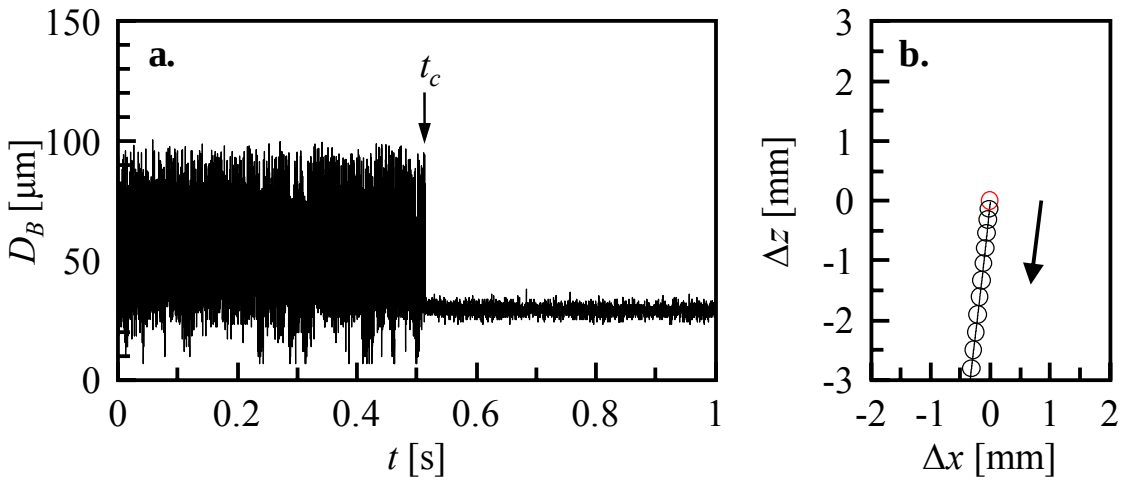

Fig. 17. Visualization results of the PSP's position change and the ACOB's diameter under S2. **a:** ACOB's diameter. **b:** PSP's position change.

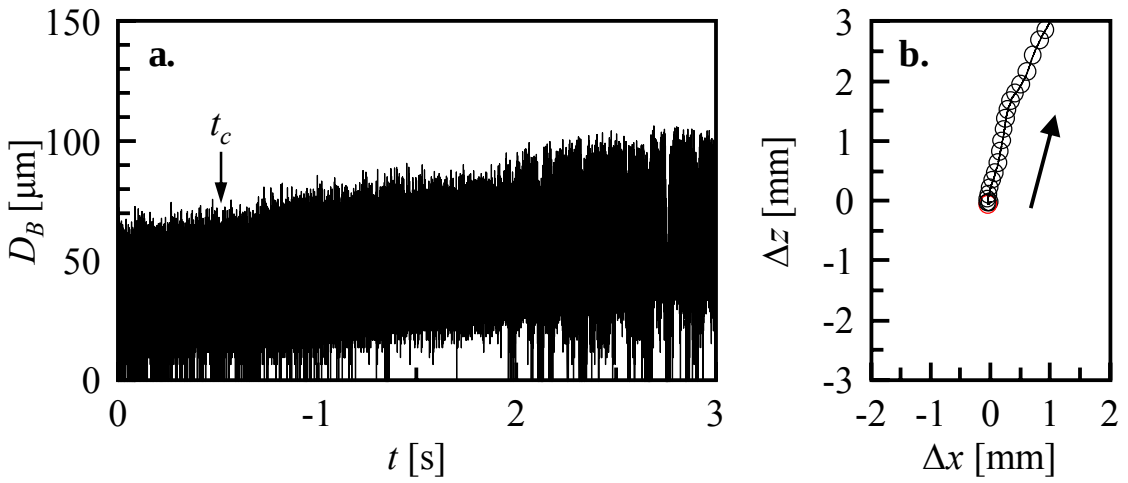

Fig. 18. Visualization results of the PSP's position change and the ACOB's diameter under G1. **a:** ACOB's diameter. **b:** PSP's position change.

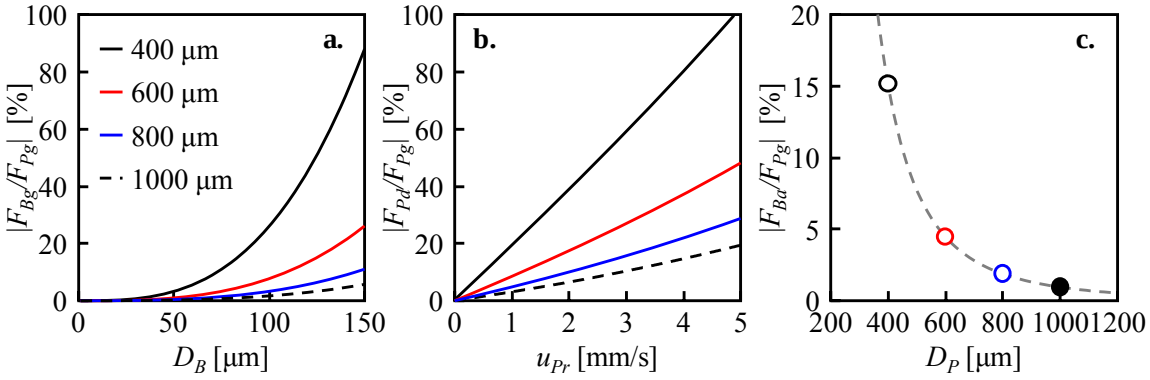

Fig. 19. The ratios of the forces to F_{Pg}. **a:** F_{Bg} vs. F_{Pg}. **b:** F_{Pd} vs. F_{Pg}. **c:** F_{Ba} vs. F_{Pg}.

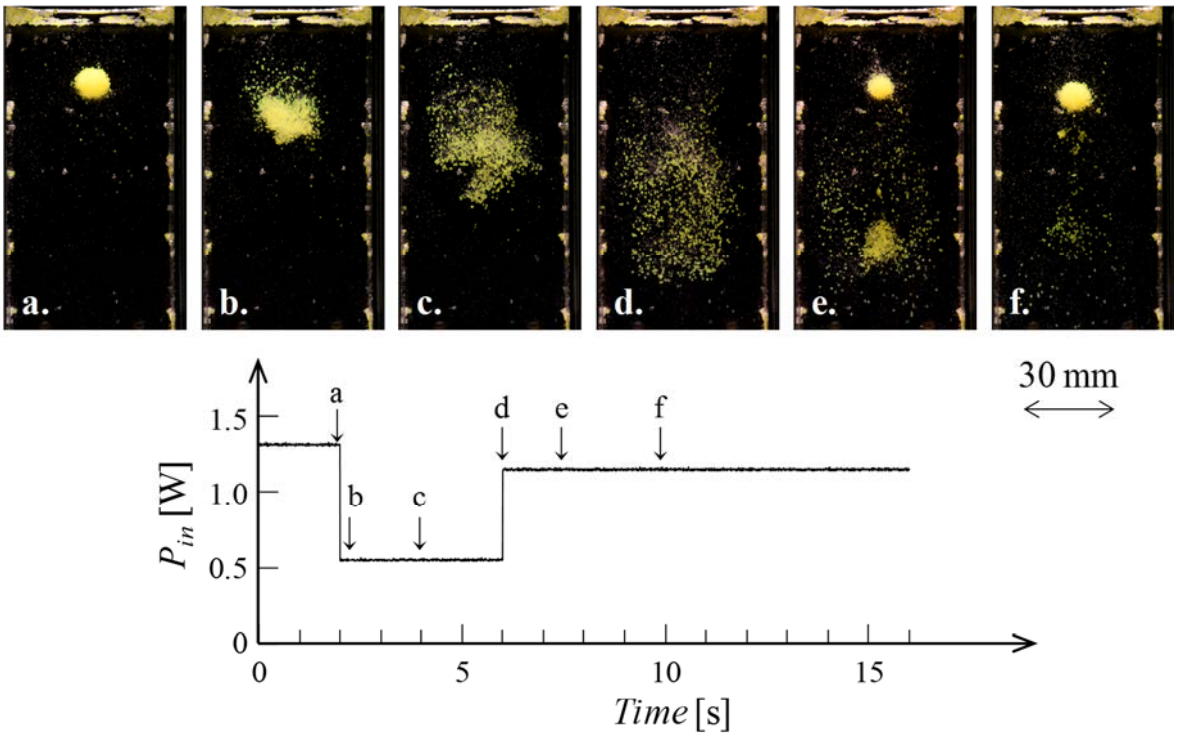

Fig. 20. Particle classification process under the step-like amplitude change of P_{in}, and P_{in} vs. time. *White particles:* dia. 400 μm, density 1060 kg/m^3. *Yellow particles:* dia. 800 μm, density 1060 kg/m^3.

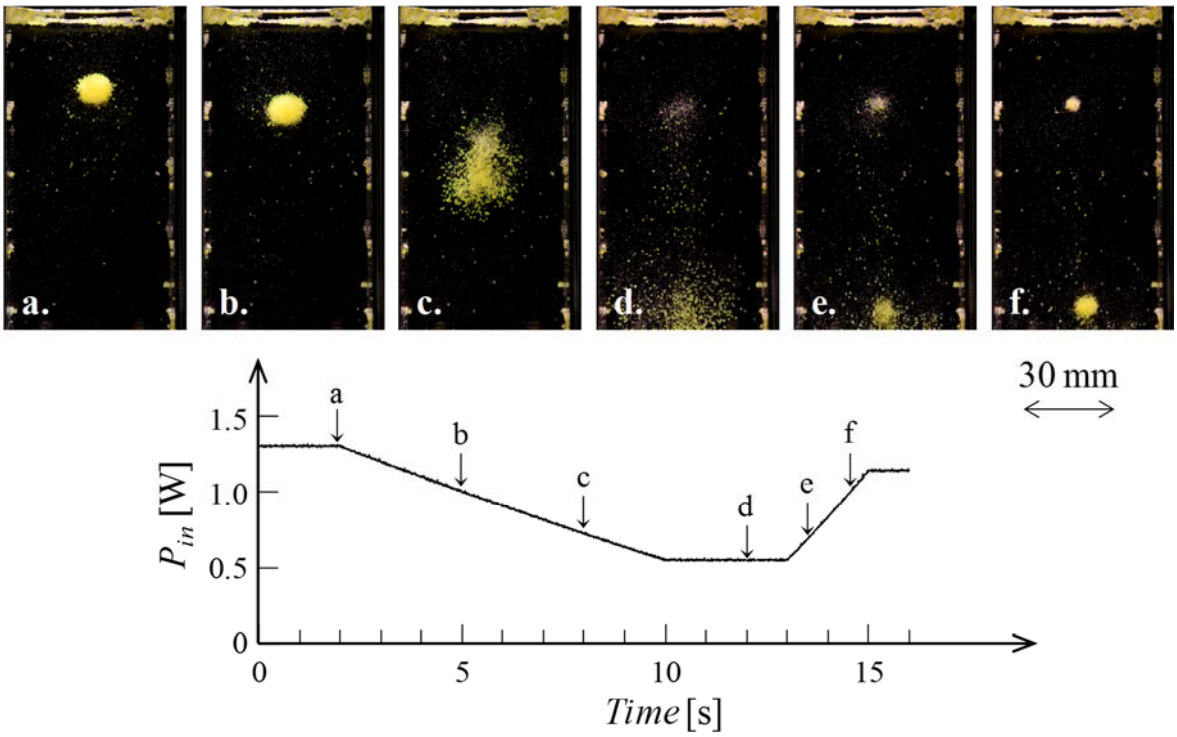

Fig. 21. Particle classification process under the gradual amplitude change of P_{in}, and P_{in} vs. time. *White particles:* dia. 400 μm, density 1060 kg/m^3. *Yellow particles:* dia. 800 μm, density 1060 kg/m^3.

Table 1. Experimental conditions under the transition state in the input power.

Condition	Change pattern in P_{in}	P_{in} before amplitude change [W]	P_{in} after amplitude change [W]	dP_{in}/dt [W/s]	$\overline{u_P}$ [mm/s]
G1	Gradual change	1.75	1.09	−0.33	3.21
G2	Gradual change	1.75	1.09	−0.17	2.17
G3	Gradual change	1.75	1.09	−0.08	1.31
S1	Step-like change	1.75	1.09	$-\infty$	−11.8
S2	Step-like change	1.75	0	$-\infty$	−12.4